Determining Desired Sorbent Properties for Proton-Coupled Electron Transfer-controlled CO_2 Capture using an Adaptive Sampling-Refined Classifier

Jonathan Boualavong[†a,*], Kostas Papakonstantinou[a], Christopher Gorski[‡a,*]

[a] *Department of Civil & Environmental Engineering, Pennsylvania State University, 212 Sacket Building, University Park, PA 16802, USA*

Abstract

Electrochemical CO_2 capture technologies have been found to consume less energy than the industry standard of thermal separations, but their real-world applicability requires that they also operate at comparable rates. Optimizing for both low energy demands and high capture rates is complicated by trade-offs between the two objectives and the many manipulable solution chemistry variables, including species type and concentration. Here, we computationally identified the solution chemistries that are most likely to outperform thermal separations in both energy demand and capture rate for electrochemical capture driven by proton-coupled electron transfer reactions by using an adaptive sampling contour estimation method. This approach provided high confidence inferences with few simulation runs by selecting the most informative conditions to test. We found that moderately basic pK_a values of the reduced form of the redox-active compound were the most important variables for low energy and high rate CO_2 capture.

*Corresponding authors: [†]Present address, [‡]Permanent address

Email addresses: jkb56@psu.edu (Jonathan Boualavong[†]), gorski@psu.edu (Christopher Gorski[‡])

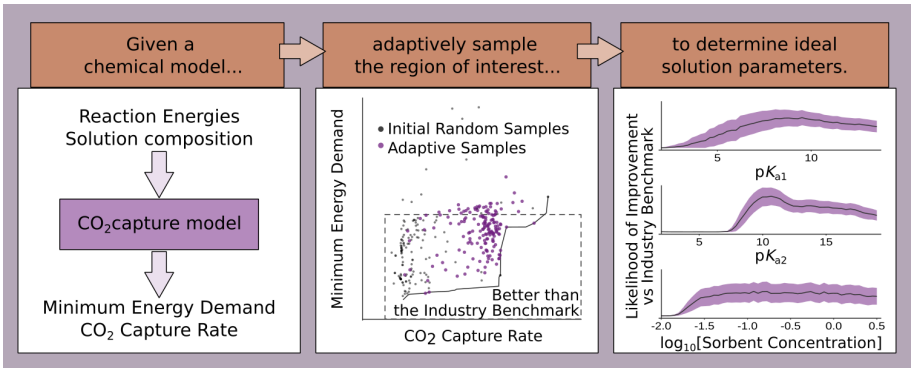

Keywords: process optimization, Gaussian process, exploitation-exploration dilemma, carbon capture, redox chemistry, pH swing

---

Abbreviations

CVI_i	Classifier variable importance of the i^{th} variable
DIC	Dissolved inorganic carbon
EFF	Expected feasibility function
GP	Gaussian process
MEA	Monoethanolamine
PCET	Proton-coupled electron transfer
SUR	Stepwise uncertainty reduction
SVM	Support vector machine
wIMSE	Weighted integrated mean square error

1. Introduction

Carbon capture technologies must become less expensive to achieve international climate goals [1, 2, 3, 4, 5]. Currently, carbon dioxide is captured at a limited number of industrial plants using the monoethanolamine (MEA) process, in which temperature swings control CO_2 absorption into and desorption from aqueous solution [6]. More widespread use of the MEA process is technologically limited by the large energy demand required for heating and cooling sorbent solutions [7, 8, 9, 10]. Theoretically, electrochemical CO_2 capture technologies can be designed to operate with lower energy requirements than

temperature-swing CO_2 capture technologies because they are not bound by the Carnot cycle [11, 12, 13]. However, most experimental electrochemical CO_2 capture systems have not yet achieved substantially lower energy demands than the MEA benchmark after accounting for typical thermal-to-electrical energy conversions [14, 15, 16, 17, 18, 19, 20, 21], and capture rates for electrochemical CO_2 capture are rarely measured using conditions that allow direct comparison to other CO_2 capture methods due to reactor design and operation differences [17, 19, 22, 23, 24]. Given that capture rates affect absorber size and therefore capital cost [5, 21, 25], we see a need to study the trade-offs that exist between minimizing energy demands and maximizing the capture rates. In this study, we focus on optimizing the solution chemistry composition for low energy demands and high capture rates because the solution composition places physical limits on what is achievable by changing, for instance, the thermodynamic minimum energy and sorbent availability [11, 12].

Identifying optimal solution compositions for electrochemical CO_2 capture can be prohibitively time-consuming for two reasons. First, a large number of manipulatable variables exists, including the concentration and species of each constituent present in solution. For electrochemical CO_2 capture technologies with many candidate compounds, the scale of these experimental designs can usually only be achieved at reasonable timescales with simulation studies. Second, we are simultaneously considering two performance metrics: energy demands and CO_2 capture rates [26, 27]. The existence of multiple objectives means there is no singular optimum, but rather there is a set of potential trade-offs between those objectives called the Pareto front [28, 29, 30, 31]. Each point on the Pareto front can be thought of as its own single-objective problem, leading to experiment designs with many conditions to test.

While various adaptive sampling methods for finding Pareto fronts have been

designed to reduce the number of tested experiment conditions, they assume a well-defined input space in which all possible input configurations are known [32, 33, 34, 35, 36, 37, 38, 39]. When optimizing a solution composition, knowing all possible input configurations would mean that almost all candidate compounds and their relevant properties are known *a priori*. Unfortunately, this is not the case for electrochemical CO_2 capture systems. Our literature survey revealed that the number of candidate compounds with both electrochemical and CO_2 capture data is on the order of 10^2, so relying solely on this data to identify the Pareto front would only reveal the best solution composition among those likely already reported in the literature. This case differs from literature examples of applying adaptive sampling methods for Pareto front estimation in other materials problems, which identify promising candidates from databases containing $>10^4$ species [40, 41, 42]. Additionally, conclusions obtained from large datasets ($>10^5$ entries) have been shown to still be susceptible to database biases [43], putting into further question the validity of any Pareto front obtained from $\approx 10^2$ candidates using any of these adaptive sampling methods.

One way to address multi-objective solution composition optimization problems when only a small fraction of candidate compounds have sufficient data is to treat each solution property as a continuous variable, then search for combinations of solution properties that produce outcomes that are sufficienciently close to the Pareto front. Treating each solution property as a continuous variable accounts for potential candidate compounds that lack measured data, and accepting results within some proximity of the Pareto front increases the likelihood that a yet-unreported compound may have a combination of properties that falls within that domain. Reframing the problem in this way changes it from a multi-objective optimization problem to a binary classification problem in which one searches for conditions that would be acceptably close to the

proposed Pareto front. While a binary classifier could be trained solely using randomly sampled conditions, the classifier is most likely to make errors in the region close to the boundary between "acceptable" and "unacceptable" CO_2 capture energies and rates, and thus the dataset should prioritize that boundary through a process called contour estimation. Like searching for a Pareto front, contour estimation is often intractable and frequently addressed through adaptive sampling [39, 44].

Conceptually, adaptive sampling algorithms for contour estimation seek to sample the point on the current estimate of the boundary that is farthest from any previous sample [45]. More sophisticated and efficient algorithms, such as the expected feasibility function (EFF) [46, 47] and the weighted integrated mean square error (wIMSE) acquisition function [48], use uncertainty estimates from Gaussian processes to account for the fact that changes in one variable may be more impactful than equivalent changes in another. Importantly, none of the contour estimation methods described here were initially designed for nor tested with boundaries that describe multiple criteria like our study, which considers both energy demands and capture rates. Because each criterion would produce its own boundary, the combined boundary describing solution chemistry conditions that meet both criteria is likely to be a piecewise function, and, to the best of our knowledge, there is no established method in the literature for estimating this piecewise boundary more efficiently than solving each criterion's boundary independently, effectively doubling the computation time for a two-criteria contour estimation problem. As the number of relevant criteria increases, this process becomes increasingly expensive. To address this knowledge gap, we developed our own adaptive sampling method that generalizes features of the wIMSE and EFF methods to refine the estimate of a boundary defined by a multi-objective problem. We use the resulting sampled dataset to produce

a classifier that gives the probability of meeting both criteria, and we show that the classifier becomes more accurate with each sampling iteration.

After initial validation of our approach with mathematical test scenarios, we applied the method to search for the optimal solution chemistry properties for CO_2 capture by pH swings generated from proton-coupled electron transfer (PCET) electrochemical reactions [11, 23, 49]. In this reaction scheme, a redox-active molecule will be electrochemically reduced and protonated; for this study, we focus on the reduction of a quinone, Q, to a hydroquinone, QH_2):

$$Q + 2H^+ + 2e^- \rightleftharpoons QH_2 \tag{1}$$

Because the total dissolved CO_2 concentration (*i.e.*, $[H_2CO_3]$ + $[HCO_3^-]$ + $[CO_3^{2-}]$) is pH-dependent, raising the pH via electrochemical reduction captures CO_2, and lowering the pH via electrochemical oxidation releases CO_2. While many other electrochemical CO_2 capture methods have been reported in the literature [15, 16, 17, 18, 19, 22, 24, 50, 51, 52, 53, 54], we chose PCET-driven pH swings as a starting point because a computational model for this system had been previously reported by Jin et al. [11], providing us with a benchmark for model validation. Additionally, this electrochemical approach depends on only four variables and takes less than one minute to calculate both energy demand and capture rate, in contrast to, for instance, the computational model for the electrochemically mediated amine regeneration mechanism [12, 55], which depends on at least nine variables for a complete description of the process and takes substantially longer to solve numerically. While Jin et al.'s model omitted the (de)protonation reactions of the reduced hydroquinone for simplicity [11], we included these reactions in our model because recent work on a different pH-controlled CO_2 capture process indicated that the lowest energy demands occurred at a moderately basic pK_a value, making these

reactions relevant under typical CO_2 capture pH conditions [13]. This optimum occurred when maximizing the overlap between the buffer regime of the sorbent species and the operating pH of the process, thereby maximizing the difference in aqueous phase CO_2 capacity between the capture and release stages. Based on similarities between these two capture mechanisms, we hypothesized that the pK_a values of the reduced species in the PCET-driven pH swing capture process would have a high impact on energy demands.

In addition to studying energy demands, we used the average flux of CO_2 in the absorber as a proxy for the rate of CO_2 capture because this is typically the rate-limiting step [20]. In the electrochemical CO_2 capture literature, the rate of capture is either omitted from study or reported from measurements that are sensitive to the reactor configuration and operation [17, 19, 22, 23, 24], making it difficult to make comparisons among studies. For our study, we applied the widely-used van Kevelen and Hoftijzer model of gas absorption with chemical reaction enhancement to obtain an upper-bound for the CO_2 flux across the vapor-liquid interface [20, 56, 57, 58, 59, 60, 61, 62]. Based on this model, we hypothesized that the rates will be higher not only at higher concentrations, but also at higher hydroquinone pK_a values because the maximum operating pH increases with pK_a [11], thereby increasing the effective sorbent concentration.

We describe here validation studies of our computational approach and its application to CO_2 capture by PCET-driven pH swings. We first introduce our computational approach, including the mathematical bi-objective test scenarios, the possible definitions of region "close to the Pareto front," and the test metrics we used when evaluating our adaptive sampling method (Section 2). We also detail our framework for interpreting the results based on partial variable dependence [63, 64] and variable importance [65, 66, 67]. Overall, we found that our adaptive sampling approach produced a more accurate classifier compared

to an equivalent number of solely random samples, particularly as the test scenario became more complex (Section 3). Next, we describe how we applied this method to our CO_2 capture model to search for the solution composition that would produce energy demands and CO_2 capture rates competitive with that of the MEA-based temperature-swing benchmark (Section 4). We found that while this electrochemical process can be competitive with the MEA benchmark, particularly in achieving lower energy demands, the range of potential energy demands and rates was large, with a substantial fraction of possible solution compositions failing to capture CO_2 at all (Section 5). Based on our results, we provided suggested domains for the hydroquinone pK_a values, total quinone concentration, and magnitude of any pH correction to aid in implementation of this process. Finally, we applied our model to literature data of substituted hydroquinones to identify trends in how the functional group substitutions affect predicted performance.

2. Computational Approach

2.1. Overview

We describe here a method to identify the domain of conditions whose outcomes were "sufficiently close" to the Pareto front. This method first produces an estimate of the Pareto front using an established process [68], then applies our new contour estimation method to find a specific contour of interest relative to that Pareto front estimate. We estimated both the Pareto front and the contour of interest using the same basic procedure: (*1*) collect an initial set of data, (*2*) use the sampled data to fit a surrogate model that is easier to evaluate than the objective functions (Section 2.2), (*3*) apply an acquisition function to the surrogate model to determine the point that would improve the estimate of the Pareto front or contour the most (Section 2.3), (*4*) evaluate the objective

functions at this point, and (*5*) repeat steps 2-4 until a predefined convergence is met or a maximum number of samples were collected. For Pareto front estimation, the initial set of data combined a grid search with random sampling, and for contour estimation, the initial set of data was the dataset after Pareto front estimation.

The adaptively sampled dataset was then used to train a classifier, which predicted whether an input vector would produce an outcome sufficiently close to the Pareto front or not. We could then analyze this classifier to infer information about the original objective functions with reduced computational cost compared to evaluating the objective functions directly. The utility of these inferences depended on the accuracy of the classifier, which itself depended on the quality and quantity of sampled data used to train it. Therefore, to confirm that our adaptive sampling method for contour estimation was beneficial to the accuracy of the classifier, we applied our methods to two simple mathematical test scenarios and three possible definitions of the region "close to the Pareto front." We compared the accuracy of classifiers trained on adaptively sampled data to the accuracy of the same classifier trained on an equivalent number of solely random samples, with the expectation that the more informative adaptive sampling procedure would produce more accurate classifiers. Finally, we developed methods for interpreting those classifiers in ways that would be useful for our goal of optimizing solution compositions for electrochemical CO_2 capture.

2.2. Gaussian Process Surrogate Model Construction

We used Gaussian processes (GP) as the surrogate model for estimating both the Pareto front and the contour of interest because our data were derived from deterministic models. While many potential alternative surrogate models, such as general linear models or random forests [69, 70, 71, 72], rely on minimization of the differences between the model prediction and sampled

data to find generalized trends, GP can use Bayes' rule to find the posterior distribution conditioned on the sampled data, assuming a Gaussian prior [73]. As a result, at a sampled datapoint ($\bar{x}_n$, $f(\bar{x}_n)$) from a deterministic function with high precision (*i.e.*, $(\bar{x}_n) << |f(\bar{x}_n)|$), the GP surrogate model intersects the sampled data points with similarly high precision. In other words, errors in the surrogate model were predominantly due to surrogate model inaccuracies, not measurement imprecision as could be assumed in least-squares regression surrogate models [46]. This feature also ensured that in the proximity of a sampled point, the model uncertainty was small, but the domain far from any samples had larger uncertainty based on that distance. Thus, a GP surrogate gives information on both exploration of new areas and exploitation of known information for the adaptive sampling algorithm.

The fitted GP surrogate model ($g(\bar{x})$) predicts both the mean ($\mu(\bar{x})$) and variance ($\sigma^2(\bar{x})$) of the output given an input vector ($\bar{x}$) (Eq. 2).

$$g(\bar{x}) \sim N(\mu(\bar{x}), \sigma^2(\bar{x})) \tag{2}$$

Further details on fitting the mean and variance to data have previously been reported in the literature [33, 74, 75], and implementation packages in various programming languages are available [76, 77]. Briefly, after selecting a covariance function, the most probable GP surrogate model's mean and variance can be calculated by fitting to the sampled data [74]. For this study, we did not notice a substantial difference among different covariance functions and chose the 5/2 Matern covariance function due to its comparatively faster fitting of preliminary test data.

2.3. Bi-Objective Problem Acquisition Functions

To estimate the Pareto front, we used the stepwise uncertainty reduction (SUR) acquisition function [32] generalized to multi-objective problems [33], as implemented in the GPareto package (v.1.1.4.1) in R (v.4.0.3) [68]. In this method, the two objective functions were assumed to be uncorrelated minimization problems and thus produced two independent GP surrogates [68, 78]. While the independence assumption may not apply to all bi-objective problems, the outputs of our chemical model showed little correlation (Pearson's $|r| < 0.01$). At each iteration, GP surrogates models for each objective were queried to find the next candidate point that would offer the greatest expected increase in the 2-dimensional area behind the bi-objective Pareto front estimate. If the point would be less optimal than the estimated Pareto front, this area would be unchanged; if the candidate was more optimal than any points on the estimated Pareto front, the area would increase. Maximizing this expectation value accounted for both the means and variances of the two GP predictions, favoring regions that are both promising in their means and comparatively unexplored as noted by high uncertainty. The SUR method specifically aimed to pick samples that will maximize Shannon information entropy in order to minimize uncertainty of the Pareto front estimate [33].

To improve our estimate of the contour that defines points that are sufficiently close to the Pareto front, we developed an adaptive sampling method that sampled the regions that are both highly uncertain and close to the classification boundary of interest by generalizing features of the expected feasibility function (EFF) and the weighted integrated mean square error (wIMSE) methods [46, 47, 48]. Instead of using a binary inequality of a single GP surrogate like the EFF and wIMSE methods, we converted the continuous outputs of the relevant GP surrogates into a single probabilistic classifier that gives the

joint probability of meeting all specified selection criteria conditioned on the input vector $(P|\bar{x})$. The boundary can then be defined as the domain where the probability is 0.5, described mathematically as maximizing $(P|\bar{x})(1-P|\bar{x})$. To calculate the joint probability of meeting all criteria, we assumed all surrogate model outputs were independent, similar to the estimation of the Pareto front, so for multiple selection criteria, the joint probability was the product of the probabilities of meeting each separate criterion. Each individual criterion probability could be calculated from a normal distribution using the GP surrogate's mean and variance. Note that for this contour estimation process, the GP surrogates gave predictions of the outputs most closely related to the contour definition, which may not be the same as the original objective functions. For instance, if the contour of interest was defined by the sum and product of the original objective functions, the GP surrogate models would be trained on the sum and products themselves to eliminate the need to propagate the surrogate model uncertainties, particularly if the transformation would convert the output from a Gaussian into another type of probability distribution. We specifically chose the sets of selection criteria to limit their covariance and ensure our independence assumption remained valid.

The uncertainties of the multiple independent GP were combined into a single metric to account for potential differences in uncertainty among the surrogate models for each selection criterion. For this work, we used the variance of the product of the selection criteria estimated using the Taylor series approximation as an initial estimate of the total uncertainty $(\sigma_T^2(\bar{x}))$ (Eq. 3 for the 2-criteria case [79]). While more sophisticated measures of total uncertainty are possible, we picked this form for its generalizability and ease of calculation. Similarly, while integrating the uncertainty measure over the whole input space would provide a more accurate estimate of the improvement than a sample could

provide, the reduction in total variance was expected to be localized [47, 48], so we used the variance at the candidate point to reduce the computational cost of each iteration.

$$\left(\frac{\sigma_T(\bar{x})}{\mu_1(\bar{x})\mu_2(\bar{x})}\right)^2 = \left(\frac{\sigma_1(\bar{x})}{\mu_1(\bar{x})}\right)^2 + \left(\frac{\sigma_2(\bar{x})}{\mu_2(\bar{x})}\right)^2 \tag{3}$$

The most useful next sampling point, and therefore the target of the adaptive sampling method, would maximize the acquisition function, $U(\bar{x})$ (Eq. 4). Conceptually, like the EFF and wIMSE acquisition functions, this acquisition function is the product of the uncertainty and the proximity to the boundary:

$$U(\bar{x}) = \sigma_T^2(\bar{x})\ ((P|\bar{x})(1 - P|\bar{x}) + \epsilon), \epsilon \geq 0 \tag{4}$$

We introduced the constant ϵ in this work as a user-defined tuning parameter to adjust the relative weight of exploration and exploitation, similar to the β term in some Bayesian optimization literature [80, 81]. When $\epsilon = 0$, points that the GP surrogate models confidently estimated on one side of the boundary ($P|\bar{x} \approx 0$ or $P|\bar{x} \approx 1$) would have $U \approx 0$ independent of $\sigma_T^2(\bar{x})$, so maximizing U prioritized points on the boundary and favored exploitation of known information. As ϵ increases, points on the classification boundary and points farther from the boundary have more similar evaluations of $(P|\bar{x})(1 - P|\bar{x})$, leading to a prioritization of exploration by favoring points with higher total uncertainty. We found tuning ϵ to be important for objective functions whose dynamics were harder to capture with a GP trained on limited data, particularly those with multiple local extrema or rapid changes in the slope. In general, we started our sampling with a large value of ϵ ($\approx 10^{-2}$) and decreased this value to a minimum of 10^{-4} as we collected more samples. We stopped collecting additional samples either when a pre-defined maximum number of samples were collected or if the

value fo U after an iteration was less than one-tenth that of the first iteration.

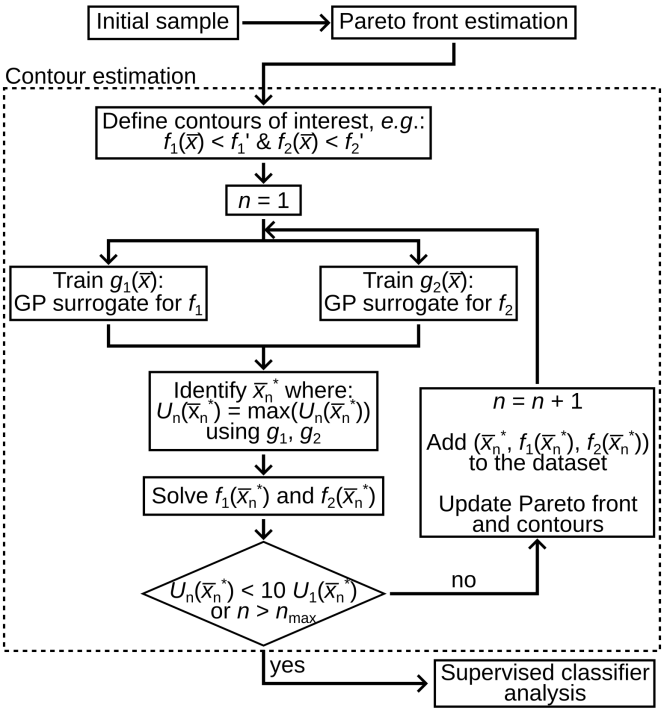

Figure 1: Flow chart of the computational approach, with details provided of our contour estimation procedure.

For all problems, we first sampled the input space composed of d independent variables with a coarse grid (3^d points) and an additional 3 points from each hypercube created by the coarse grid ($(3)2^d$ points) to ensure adequate sample coverage. We then applied the SUR algorithm to estimate the Pareto front, allowing up to as many samples as the initial design. This dataset with the refined Pareto front estimate was used as the starting dataset for the contour estimation function, with each sampled point from the contour estimation method also updating the Pareto front as appropriate (Figure 1). For the test scenarios, the adaptive sampling step was limited to between $10d$ and $20d$ samples due to the simplicity of these functions; for the PCET optimization problem

this increased to $25d$ to improve confidence in our conclusions (Section 4).

2.4. Variable Effects and Feature Importance

The utility of this adaptive sampling procedure was in its ability to produce accurate classifier models despite being trained on a limited number of samples. We were specifically interested in interpreting the classifier for the impact of each individual variable and what values those variables should take in order to be close to the Pareto front. We calculated the impact of each variable on the classifier by marginalization of the joint probability (Eq. 5),

$$P|x_i = \int_{X_{-i}} (P|x_i, \bar{x}_{-i}) p(\bar{x}_{-i}) d\bar{x}_{-i} \tag{5}$$

where x_i was the value of the i^{th} input variable, $\bar{x}_{-i}$ the input vector of all variables except the i^{th} input variable, X_{-i} the set of possible $\bar{x}_{-i}$, and $p(\bar{x}_{-i})$ the probability density function of input space X_{-i} evaluated at $\bar{x}_{-i}$. $P|x_i$ represented the probability that the result would satisfy all selection criteria if only information about x_i was known, analogous to the partial dependence plots used in regression analyses [63, 64]. This integral was approximated by calculating $P|x_i, \bar{x}_{-i}$ for 1,500 Monte Carlo samples from $\bar{x}|x_i$, which, by the law of large numbers, converges to the expectation value (Eq. 6). The entire marginal was estimated from a set of 50 evenly spaced x_i values. For the test scenarios, we defined the inputs as independent variables with uniform distributions to simplify this expectation value to an unweighted average.

$$P|x_i \approx \frac{1}{N} \sum_{\bar{x}_{-i} \sim X_{-i}}^{N} P|x_i, \bar{x}_{-i} \tag{6}$$

The set of Monte Carlo samples from each evaluation of $P|x_i$ (Eq. 6) provided the additional benefit of indicating the distribution about that expectation value. The variance among the set of $P|x_i, \bar{x}_{-i}$ at constant x_i indicated how

changing the other variables in $\bar{x}_{-i}$ affected the probability that the result met the selection criteria. If the variance was small, the other variables $\bar{x}_{-i}$ did not have substantial impact on the classifier compared to x_i; at the other extreme, if the variance was large, at least one other variable had a much larger impact compared to x_i. However, this variance measure only described a single instance when x_i was set to a constant. A more useful importance measure of the variable x_i should also consider how this variance changes as x_i changes. We defined this marginals-based classifier variable importance of the i^{th} variable (CVI_i) as the ratio of the range of $P|x_i$ divided by the average of the standard deviations (Eq. 7). By having the numerator be the range of $P|x_i$, we ensured that input variables that caused large changes in the probability of acceptance were evaluated as more important.

$$CVI_i = \frac{\max(P|x_i) - \min(P|x_i)}{E_{x_i}[Var_{x_{-i}}[P|x_i, \bar{x}_{-i}]]^{0.5}} \tag{7}$$

2.5. Validation Test Scenarios

To validate our adaptive sampling and classifier variable importance methods, we applied this approach to two bi-objective problems from the literature, adapted to address particular questions we had about the suggested contour estimation approach. Both problems were selected due to their simplicity and, after modification, presence of both a global optimum and at least one other local optimum. The simplicity allowed us to evaluate the objective functions quickly in order to obtain measures of accuracy and accelerate algorithm tuning. The presence of multiple local optima was important for testing robustness to regions of acceptance that were not simply a radius around the single optimum, which could be possible as the number of variables increases in future studies of other electrochemical CO_2 capture chemistries.

The first test scenario was a modified version of the 2-input set of quadratic

polynomials from Marler & Arora [34], adjusted so that the objectives were quartic with respect to the second input variable and slightly rotated by $\theta = \frac{-\pi}{24}$ radians in the second objective by left multiplying the input vector $[x_1, x_2]^T$ by the rotation matrix $R(\theta = \frac{-\pi}{24})$ (Eq. 8). The higher order polynomial terms did not substantially affect the location of the Pareto front nor the vicinity local to the Pareto front (Figure S1a), but led to a secondary local optimum. The rotation applied to the second objective function ensured that the two local optima did not perfectly overlap at the same value of x_1, and therefore gave x_1 multiple local optima without needing to increase it to a quartic polynomial as well.

$$
\begin{aligned}
f_1(x_1, x_2) &= 20(x_1 - 0.75)^2 + 190 + 11.58x_2^4 - 115.85x_2^3 + 383.13x_2^2 - 463.5x_2 \\
[x_1', x_2']^T &= R(\frac{-\pi}{24})[x_1, x_2]^T \\
f_2(x_1', x_2') &= (x_1' - 2.5)^2 + 80 + 1.778x_2'^4 - 20x_2'^3 + 78.573x_2'^2 - 124.664x_2' \\
x_i &\in [0, 5] \forall i
\end{aligned}
\tag{8}
$$

The second test scenario was based on the ZDT4 function (Eq. 9) [38], modified in the second objective to have a lower frequency such that the gradients were more similar to preliminary calculations of the PCET system (Figure S1b-S1c). The lower frequency guaranteed that in all selection criteria that we tested, the set of accepted points was discontinuous around the three prominent local minima in f_2. While the ZDT4 function has been used with up to six input variables, we performed tests with only three inputs to serve as a transition from the two-input quartic polynomial and the four-input PCET system.

$$
\begin{aligned}
f_1(x_1, x_2, x_3) &= x_1 \\
h(x_2, x_3) &= 21 + \sum_{i=2}^{3} (0.5x_i - 0.25)^2 - 2.5\cos((5x_i - 2.5)\pi) \\
f_2(x_1, x_2, x_3) &= h(x_2, x_3)\left(1 - \sqrt{\frac{x_1}{h(x_2, x_3)}}\right) + 10\sum_{i=2}^{3}(x_i - 0.5)^2 \\
x_i &\in [0, 1] \forall i
\end{aligned}
\tag{9}
$$

Three types of selection criteria were tested as definitions for results close to the Pareto front: normalized distance from the Pareto front ("Pareto distance"), two independent thresholds for f_1 and f_2 ("Threshold cutoff"), and normalized distance to a "utopia point" criterion while prioritizing one objective more than the other ("Utopia distance") (Figure 2a). We used the standard normalization convention of (f_1, f_2) to (f_1^*, f_2^*) where the normalized single-objective optima are located at (0,1) and (1,0). This defines the point (0,0) as the utopia point, the purely theoretical point at which all objectives were optimized simultaneously [35, 36, 37, 82, 83]. For the Pareto distance criteria, the normalized distance to the Pareto front was defined as the Euclidean distance (δ) between the suboptimal normalized point and the point on the Pareto front estimate with the same $f_1^* : f_2^*$ ratio, linearly interpolating the Pareto front estimate as needed. This definition of the selection criteria reduced the two objective functions into a single criterion to search for points that were nearly Pareto optimal, accepting points with δ less than some cutoff distance δ'. For the Threshold cutoff criteria, points were accepted if each objective met a predefined independent inequality, *i.e.*, $f_1 < f_1'$ and $f_2 < f_2'$. The Threshold cutoff criteria is the simplest selection criteria and most likely to be applied in practice because design targets, such as monetary or regulatory constraints, are often defined in this way [28, 29, 30, 31]. The Utopia distance criteria accepted points that were

both within a specified normalized distance of the utopia point and satisfied the inequality $\tan^{-1}(f_2^*/f_1^*) > \theta'$. These criteria sought points that approached the utopia point as closely as possible, ignoring the shape of the Pareto front, and also rejected outcomes that favored minimizing f_2 too heavily over f_1, simulating a pre-defined prioritization preference between the two objectives. For all three selection criteria, we set the cutoff values of each criterion such that they accepted similar percentages of the input domains. For both test scenarios, the domains that met the Pareto distance and Threshold cutoff criteria were nearly identical. As a result, comparing the performance of these two selection criteria allowed us to determine whether reducing the number of GP surrogate models used in the contour estimation procedure, and thus reducing the computation time, had any measurable effect on accuracy.

We tested all combinations of the two test scenarios and the three selection criteria by comparing the results of a classifier trained on the adaptively sampled data to the results of the actual objective functions by direct evaluation. In the case of a classifier like the GP surrogates where the output is the probability of acceptance and not a direct class assignment, the accuracy assumes random assignment based on that resultant probability. We compared this accuracy to that of the classifier trained on the starting dataset prior to adaptive sampling (*i.e.*, after the Pareto front search), as well as to classifiers trained on the starting dataset combined with an equivalent number of solely random samples. These two comparisons gave insight into whether the misclassification errors improved due to adaptive sampling or the increase in training dataset size. We additionally calculated false positive and false negative error rates and single variable marginals of the classifiers to diagnose whether the misclassification errors were due to accepted regions that were too big, too small, or skewed.

For this study, we tested the accuracy of using the GP surrogate as a prob-

abilistic classifier and benchmarked it against two support vector machines (SVM), one with a 3^{rd} order polynomial kernel and one with a radial kernel, due to our unconventional use of GP surrogates as classifiers. SVM with a sigmoidal or linear kernel were initially included in the study, but showed worse accuracy than random classification assignment and were subsequently excluded. This comparison of different classifier models was intended to test (*a*) whether the GP was at least as good as a typical classifier model like SVM, reducing the computation time by using the model we already trained during adaptive sampling, and (*b*) whether the contour estimation adaptive sampling procedure would improve classifier accuracy for surrogate models besides the GP used in the sampling procedure. We specifically chose SVM due to comparatively fast fitting relative to GP in preliminary tests, particularly for larger training datasets.

To validate our proposed marginals-based contour variable importance method, we compared our metric to the Shapley values and the total-effect Sobol indices as alternatives metrics [66, 67], both of which were calculated by Monte Carlo estimation (n = 1,500). All three metrics quantify the importance of a variable in determining the outcome, in this case defined as the classification result, although they define importance differently. Shapley values describe the impact that changes to a single variable will have on the outcome relative to a reference point, while total-effect Sobol indices describe the contribution that a variable has to the variance of the output. Both Shapley values and total-effect Sobol indices were calculated 50 times to obtain an average and standard error for each input variable, and thus were determined from the same number of surrogate function evaluations as our marginals-based CVI_i metric. Uncertainties for the CVI_i metric were calculated by propagation of the standard errors of each component in Eq. 7 to obtain the standard error of the mean. Because

all three metrics define importance differently, we only compared the relative ranking of the variable importance and compared that ordinal ranking to our expectation based on the true objective functions; ideally, all three methods would agree in the ordinal ranking of the variables, although the magnitude of the differences among variables may differ.

3. Validation of Adaptive Sampling Method

Given the relative simplicity of the 2-input quartic polynomial test scenario, we only report here the results for the more complex 3-input modified ZDT4 test scenario. Results for the polynomial test scenario generally corroborated the conclusions we reached using the ZDT4 test scenario (Supplemental Information B). For the modified ZDT4 tests, we designed the selection criteria to only accept a small (5 - 10%) fraction of the input domain to be consistent with our intended application of optimization, contrasting with approximately 40% for the 2-input polynomial test scenario. This equated to accepting points that (*a*) had a normalized distance less than 0.5 from the Pareto front ("Pareto distance" criteria), (*b*) had normalized coordinates within the square defined by the utopia point and (1, 1) ("Threshold cutoff" criteria), or (*c*) were within a normalized distance of 1 from the utopia point and satisfied the inequality $\tan^{-1}(f_2^*/f_1^*) \geq 0.1$ radians ("Utopia distance" criteria).

The misclassification errors highlight the benefits of our adaptive sampling method for contour estimation on the resulting classifier (Figure 2b). For ease of visualization, we present the misclassification errors relative to those of the classifiers trained on the starting dataset without additional sampling due to differences in the starting error rates; we include the absolute misclassification error rates in the SI (Figure S2). For the GP classifier, training the models on the adaptively sampled dataset led to lower error rates than training on >95%

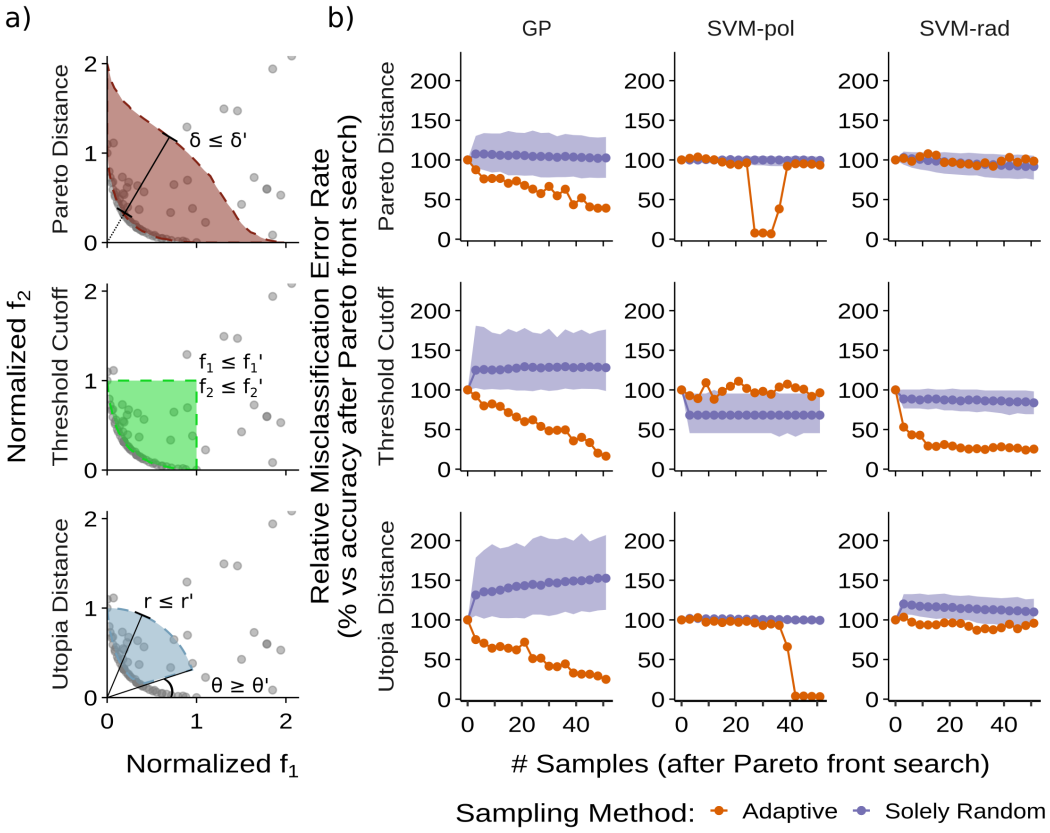

Figure 2: (a) Visual depiction of the three selection criteria. (b) Misclassification error rates, presented as a percentage of the error rate with zero additional samples beyond the starting dataset, for Gaussian process (GP) or support vector machine (SVM) models with a polynomial or radial kernel function trained on data from the modified ZDT4 test scenario. The shaded region represents the 95% confidence interval of possible solely randomly sampled training datasets, with points depicting the median (n = 1,000).

of the possible solely randomly sampled datasets, and this accuracy benefit became larger as the number of samples increased. For the SVM classifiers with polynomial kernels, the error rate stayed nearly constant with adaptive sampling unless some specific points were sampled, leading to a rapid decrease in the error rates. However, the error rate was unstable, where additional adaptive samples could potentially lead to an increase in error rates, as evident for the Pareto distance criteria. SVM with a radial kernel trained on adaptively sampled

datasets were better than >90% of solely randomly sampled datasets for two of the three selection criteria. For the Pareto distance criterion, this classifier trained on an adaptive sampled dataset was roughly equivalent to the median among the possible solely randomly sampled datasets.

We attribute the stronger benefit of adaptive sampling for the GP classifier to the fact that the adaptive sampling process used the same GP surrogate to inform the sampling process. As a result, the "most informative" next point was based on the GP's uncertainty and contour estimate, and, based on the large difference in GP and SVM classifier accuracies, this would likely be different than the uncertainty and contour estimate from a SVM given the stark differences in error rates (Figure S2). Therefore, if intending to use another type of classifier as the final surrogate model, we suggest modifying the adaptive sampling procedure to rely on information related to that same type of classifier. Using a different surrogate model for sampling may still improve accuracy of the final surrogate model, as evident in the improvement to the accuracy of SVM classifiers with radial kernels for certain selection criteria, but the benefit is likely to be smaller.

Across all selection criteria and sampling methods, the error rate for the GP classifier was always less than 10%, dropping to under 4% after 50 adaptive samples beyond the starting dataset (Figure S2). In contrast, the SVM models were inconsistent, with error rates of about 50% for most conditions tested regardless of training dataset size. Only SVM with a polynomial kernel were able to achieve error rates similar to the GP classifier, and only reliably for the Threshold cutoff condition. For the other two criteria, the error rate did drop below 10% after sufficient adaptive samples were collected, but the low error rate was unstable and rebounded back to 80% when greater than 40 adaptive samples were collected for the Pareto distance criterion. For all conditions, the misclassification errors were due to a high false positive rate (Figure S3), which

tended to be relatively high (>50%) and followed a similar trend as the total error rates when additional samples were collected. False negatives were uncommon for all conditions (<1.5%), likely a reflection of the small fraction of the input domain that met the acceptance criteria (Figure S4). Notably, adaptive sampling did not substantially improve the false negative rates compared to solely random sampling, but given the small false negative rates, reducing the false negative rate was low priority to minimize overall misclassification errors.

The single variable marginals corroborate the results of the misclassification error, showing the improvement to the GP classifiers' accuracies after adaptive sampling and the better accuracy of the GP classifiers compared to the SVM classifiers (Figure S5). While the misclassification error rates were similar among the models for the Threshold cutoff criteria after 50 adaptive samples, the (aggregated) single variable marginals for the SVM classifiers did not match expected profiles ($R^2 < 0.1$), particularly compared to the GP classifiers after adaptive sampling ($R^2 > 0.85$). This appeared to be largely due to poor marginalization on x_2 and x_3, which have distinct peaks that the SVM classifiers did not capture (Figure S6).

Given the low coefficients of determination for the SVM classifiers, we did not perform calculations for the importance ranking with these models, instead only comparing our method of assessing the marginals-based classifier variable importance to alternative importance measures for the GP classifiers (Figure 3). Our marginals-based method gave the expected ordering of the three input variables: $x_2 \approx x_3 > x_1$ across all selection criteria. The proximity of x_2 and x_3 was particularly important given that in the ZDT4 function, these two variables were treated identically, and thus should have the same importance. Additionally, in the ZDT4 function, x_1 only affected the relative balance of f_1 to f_2, but had little impact on proximity to the Pareto front [38], so we expected it

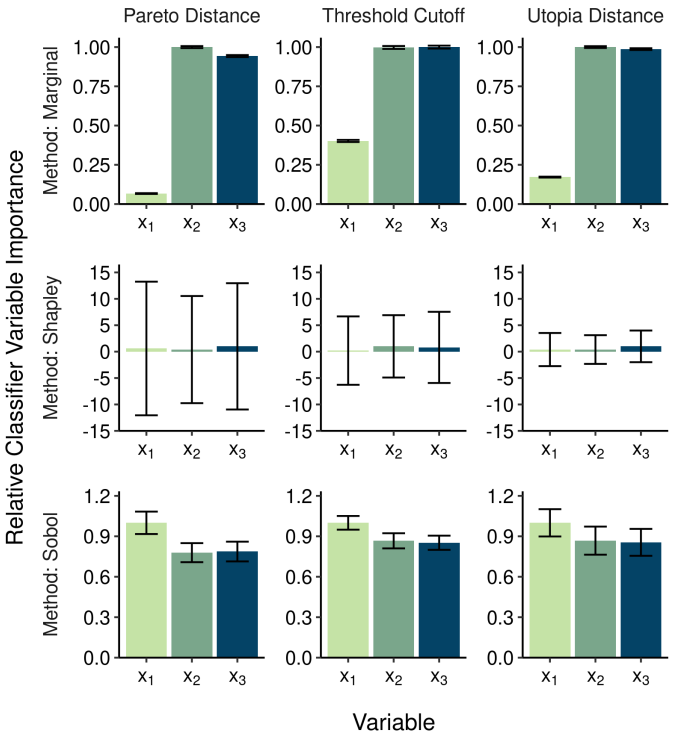

Figure 3: Normalized importance ranking for the modified ZDT4 test scenario using the marginals-based classifier variable importance, the mean Shapley values, or the total-effect Sobol index. Error bars are the standard error based on 50 independent simulations.

to have a lower importance compared to x_2 and x_3. While the Shapley value averages matched the expected order, they were poorly reproducible, leading to a large standard error that masked interpretability; in contrast, the standard errors for our marginals-based method were negligible. Total-effect Sobol indices produced more reliable results than Shapley values, but they rank x_1 as the most important variable instead. This highlights the key difference between the Sobol indices and our marginals-based method. The total-effect Sobol indices rank variables by their contribution to the output variance normalized by the total output variance, but our marginals-based metric is the probabilistic output range normalized by the variance of other variables. While the difference in the

denominators is only likely to affect resolution, the difference between variance and range of the probability in the numerator can cause a reversal in the order. Specifically, while the ranges of $P|x_2$ and $P|x_3$ were roughly double that of $P|x_1$ (Figure S6), because $P|x_2$ and $P|x_3$ were mostly flat with three relatively sharp and narrow peaks, the variance contribution of x_2 and x_3 is smaller than x_1. If these peaks were to maintain the same amplitude but have narrower nonzero domains, we would suggest constraining these two variables to the domain of those peaks with even higher priority, but their total-effect Sobol indices would decrease. In other words, here, the total-effect Sobol index can underestimate the importance of variables that have small subdomains of interest, leading to a different ordinal ranking compared to the other two metrics. Based on other experiments in the literature [13], we hypothesized that the equilibrium constants in the CO_2 capture system will have clearly defined optima at moderate values, for which the total-effect Sobol indices could underestimate their importance, so we used our marginals-based contour variable importance metric.

Collectively, these results indicated that the GP probabilistic classifier becomes significantly more accurate with adaptive sampling, reducing the number of queries of the original objective functions to achieve a surrogate model of comparable accuracy, and a GP classifier was more accurate than the tested SVM. From the tests of different selection criteria, we determined that selection based on cutoff values of the two objectives was most consistently accurate for the two test scenarios. Based on these results, we applied these methods to our analysis of the PCET-based CO_2 capture system to determine the solution chemistry properties that would be competitive with the industry benchmark: capture by temperature-swing of MEA solutions.

4. CO_2 Capture Model

4.1. Solution Chemistry Model

While CO_2 capture by PCET-driven pH swings is controlled externally by the redox reaction (Eq. 1), a complete understanding of the process includes vapor-liquid equilibrium and (de)protonation reactions (Eq. 10-15). We note that while deprotonated hydroquinones have been reported to coordinate with CO_2 directly by acting as a nucleophile, this has only been observed in aprotic solvents, so we did not include this species in our aqueous solution chemistry model [15, 84, 85, 86]. Additionally, based on data of quinone reduction potentials [87], we ignored all reactions involving singly-reduced semiquinone intermediate because for the expected pH window of operation, the second reduction potential was energetically downhill after the first electron has been accepted for the majority of species. While we expect realistic implementation would include high ionic strength to reduce the solution resistance, we simplified the calculations by ignoring ionic strength effects and assuming activity coefficients of 1. This assumption likely changed the estimates of the optimal solution chemistry properties, but we expect the difference to be small relative to the breadth of the input suggestion domains [88]. Due to limitations on the available equilibrium constant data, we calculated CO_2 capture thermodynamics assuming a constant temperature of 298 K even though absorption often occurs at 313 K. We do not expect the temperature to substantially change results because experiments of electrochemical CO_2 capture at both temperatures indicated that the decrease in captured CO_2 was counteracted by a decrease in electrical energy consumption, leading to similar energy demands per mass of CO_2 captured [18].

Vapor-liquid reactions

$$\mathrm{CO_2(g) + H_2O(l) \overset{K_H}{\rightleftharpoons} H_2CO_3(aq)} \tag{10}$$

(de)Protonation reactions

$$\mathrm{H_2CO_3(aq) \overset{K_{ca,1}}{\rightleftharpoons} H^+(aq) + HCO_3^-(aq)} \tag{11}$$

$$\mathrm{HCO_3^-(aq) \overset{K_{ca,2}}{\rightleftharpoons} H^+(aq) + CO_3^{2-}(aq)} \tag{12}$$

$$\mathrm{QH_2(aq) \overset{K_{a,1}}{\rightleftharpoons} QH^-(aq) + H^+(aq)} \tag{13}$$

$$\mathrm{QH^-(aq) \overset{K_{a,2}}{\rightleftharpoons} Q^{2-}(aq) + H^+(aq)} \tag{14}$$

$$\mathrm{H_2O(l) \overset{K_w}{\rightleftharpoons} H^+(aq) + OH^-(aq)} \tag{15}$$

The extent of the electrochemical reaction was defined in terms of y_r, the fraction of quinone that was in any of its reduced hydroquinone forms (Eq. 16). We assumed that the solution would contain excess generic background electrolyte salt $\mathrm{M_aX_b}$, and thus as the electrochemical reaction proceeded and y_r changed, electrochemical migration between the anode and cathode would be dominated by the background electrolyte and not any of the species listed in the (de)protonation reactions. Given that the species of background electrolyte should be inert and therefore not participate in any processes besides this transport, we assumed the valence of both the background anion and cation (a and b, respectively) to be 1 for simplicity. Assuming that the solution started in the oxidized state due to the oxidizing conditions of ambient air, we related the concentration difference between the background cation and anion to y_r, the total quinone concentration $[\mathrm{Q}]_{\mathrm{tot}}$, and the amount of acid (as generic acid HX) or base (as generic base MOH) that was initially added to the solution by assuming maintenance of a charge balance (Eq. 17). For the purposes of the

model, only the difference between the cation and anion concentrations and that between the additional base and acid mattered, not their individual values.

$$y_r = \frac{[\mathrm{QH_2}] + [\mathrm{QH^-}] + [\mathrm{Q^{2-}}]}{[\mathrm{Q_{tot}}]} \tag{16}$$

$$[\mathrm{M^+}] - [\mathrm{X^-}] = [\mathrm{MOH}] - [\mathrm{HX}] + 2y_r[\mathrm{Q_{tot}}] \tag{17}$$

Using only knowledge of the total concentrations of all species, the fraction of reduced quinone, and either the CO_2 partial pressure (P_{CO_2}) or the total dissolved inorganic carbon concentration (DIC), we solved the set of mass balance, charge balance, and chemical equilibrium equations to find the concentrations of the species of interest throughout the CO_2 capture process. Based on this model, the relevant solution chemistry variables that should be optimized were the $pK_{a,1}$ and $pK_{a,2}$ of the hydroquinone, the total concentration of quinone, and the net amount of acid or base to be added. Because pH is a log scale, the concentrations needed high resolution over multiple orders of magnitude. For our optimization, we used log units of concentration to maintain an experimentally-relevant resolution throughout the entire domain, and as a result, created two different models for net acid and net base addition because net acid addition is represented as a negative number. We adaptively sampled for the Pareto front and contour estimation of these two conditions in parallel, then combined the datasets for interpretation by adding another variable for the direction of the pH correction.

4.2. Process Stages

The simulated process consisted of 4 stages: oxidative acidification, CO_2 degassing, reductive regeneration, and CO_2 capture (Figure 4). While previous calculations have found that process intensification to a 2-stage process by com-

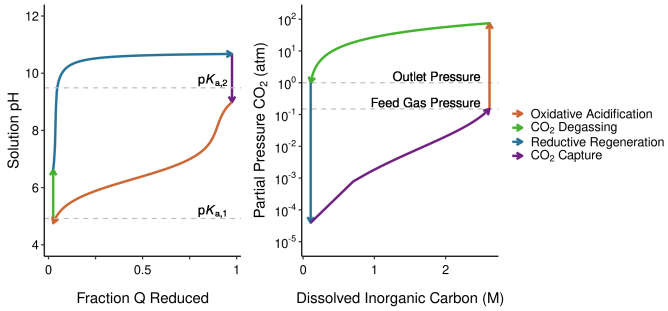

Figure 4: Representative cycles in the 4-stage CO_2 capture process by PCET-driven pH swings. (left) Changes in bulk solution pH and fraction of quinone (Q) in the reduced state compared to the reduced state's pK_a values. (right) Partial pressure of CO_2 that would be at equilibrium with the solution as the total dissolved inorganic carbon concentration changes. Outlet partial pressure: 0.99 atm CO_2. Feed gas partial pressure: 0.15 atm CO_2.

bining oxidation with degassing and reduction with capture led to lower energy demands [11, 12], this result relies on the assumption that CO_2 mass transfer across the vapor-liquid interface was fast compared to the electrochemical reactions, which cannot always be assumed to be true. Combined with the fact that the 4-stage process would give more conservative results for the energy demands, we opted for simulating the process as 4 stages in series.

The oxidative acidification stage simulation began at $y_r = 0.975$, the fully reduced extreme, at equilibrium with the inlet flue gas of 0.15 atm, solving for the pH and total dissolved inorganic carbon by solving the set of chemical equilibrium, mass balance, and charge balance equations described in Section 4.1. The proton concentration was solved numerically as the sole positive real root, and thus only valid pH, of the resulting fifth order polynomial using the Jenkins-Traub algorithm [89]. The DIC was determined using the now-solved pH and known P_{CO_2} to solve the relevant chemical equilibrium equations (Eq. 10-15). We simulated the remainder of the oxidative acidification process using 150 additional equally spaced steps along $y_r \in [0.975, 0.025]$, holding DIC constant and solving for pH and P_{CO_2}. While the electrochemical process did not

depend on P_{CO_2} directly, its knowledge at each step was used as a check that the pH, which was solved iteratively due to its nonlinear relationship with DIC and y_r, remained within realistic bounds. This calculation implicitly assumed that the (de)protonation reactions and the mixing between the electrode surface and the bulk were fast relative to the electrochemical reaction. The former can be assumed to be true due to the abundance of water molecules and its rapid proton exchange, while the latter should be valid in a well-designed electrochemical cell that minimizes mass transfer resistances.

The CO_2 degassing stage simulation started with the pH, P_{CO_2}, y_r, and DIC conditions of the final step of the oxidative acidification stage, and then it solved for pH and DIC as P_{CO_2} linearly decreased to the target outlet of 1 atm at a constant y_r using the same equation and algorithm as the first step of the oxidative acidification stage. Reductive regeneration was simulated using the same procedure as the oxidative acidification stage, but started at $y_r = 0.025$ and $P_{CO_2} = 0.99$ atm and proceeded at constant DIC until $y_r = 0.975$. Likewise, the CO_2 capture stage was simulated using the same procedure as the CO_2 degassing stage, instead ending with a $P_{CO_2} = 0.15$ atm, the assumed partial pressure of the influent flue gas.

4.3. Minimum Energy Demand

To simplify the energy demand calculation, we redefined the electrochemical reaction (Eq. 1) to its form under strongly basic conditions (Eq. 18), recognizing that the electrochemical potential was the same for the entire solution, and therefore all electrochemical reactions should be at equilibrium with each other due out assumption of fast proton exchange.

$$\mathrm{Q} + 2\mathrm{e}^- \rightleftharpoons \mathrm{Q}^{2-} \tag{18}$$

The electrical potential of the anode or cathode, E_h, over the course of the electrochemical stages were calculated using the Nernst equation (Eq. 19).

$$E_h = E_h^{0''} + \frac{RT}{2F} \ln \frac{[\mathrm{Q}]}{[\mathrm{Q}^{2-}]} \tag{19}$$

where $E_h^{0''}$ is the standard reduction potential for the doubly-deprotonated reaction in Eq. 18, R is the ideal gas constant, T is the absolute temperature, and F is Faraday's constant. Combining Eq. 19 with the identity of y_r (Eq. 16) and the chemical reactions in Eq. 13-14 produced the Nernst equation in terms of the process variables solved in Section 4.2 (Eq. 20).

$$E_h = E_h^{0''} + \frac{RT}{2F} \ln \frac{1 - y_r}{y_r} \frac{K_{a,1}K_{a,2} + K_{a,1}[\mathrm{H}^+] + [\mathrm{H}^+]^2}{K_{a,1}K_{a,2}} \tag{20}$$

The thermodynamic minimum for the electrochemical work per complete cycle per volume of solution (W_{cyc}) was calculated using the equation for electrical work from the total (positive) charge passed per solution volume (q) and cell voltage ($E_{h,\mathrm{anode}} - E_{h,\mathrm{cathode}}$) (Eq. 21). By Faraday's law of electrolysis, the charge passed was proportional to the change in the fraction of reduced quinone (Eq. 22), simplifying the electrochemical work to an integral over y_r (Eq. 23), which we solved by trapezoidal Reimann sum over the 151 steps of each of the two electrochemical stages.

$$W_{cyc} = \int_{q=0}^{q=q_{\max}} (E_{h,\mathrm{anode}} - E_{h,\mathrm{cathode}}) dq \tag{21}$$

$$q = -zF[Q]_{\mathrm{tot}} y_r \tag{22}$$

$$W_{cyc} = -zF[Q]_{\mathrm{tot}} \int_{y_r=0.025}^{y_r=0.975} (E_{h,\mathrm{anode}} - E_{h,\mathrm{cathode}}) dy_r \tag{23}$$

The total work per mole of CO_2 captured ($W_{\mathrm{CO_2}}$) was estimated as the

work per cycle per volume divided by the net change in DIC over the course of the CO_2 capture stage (Eq. 24). This approximation assumed that the pump work was small compared to the electrochemical work based on estimates of the pump work for capture with a MEA solution (< 0.5 kJ_e/mol C) [20] compared to preliminary calculations of the energy (≥ 8 kJ_e/mol C).

$$W_{\mathrm{CO_2}} \approx \frac{W_{cyc}}{\Delta DIC} \tag{24}$$

Because the energy demand should decrease as less CO_2 is removed, we added an additional scaling factor, w, to penalize the predicted minimum energy demand if less than 90% removal occurs to keep results in line with the US Department of Energy's target [10]. Doing so prevented the Pareto front search from expending computational resources finding parts of the Pareto front that would have low energy demand simply because the process captured little to no CO_2. This scaling factor was based on the minimum work of separation (W_{min}) to split the feed gas into a 99% pure outlet and a lean gas of known CO_2 partial pressure (Eq. 25).

$$\begin{aligned} W_{min}(P^{lean}_{\mathrm{CO_2}}) = RT(&-n^{feed}_{\mathrm{CO_2}} \ln(P^{feed}_{\mathrm{CO_2}}) + n^{out}_{\mathrm{CO_2}} \ln(P^{out}_{\mathrm{CO_2}}) + n^{lean}_{\mathrm{CO_2}} \ln(P^{lean}_{\mathrm{CO_2}}) \\ &- n^{feed}_{-\mathrm{CO_2}} \ln(P^{feed}_{-\mathrm{CO_2}}) + n^{out}_{-\mathrm{CO_2}} \ln(P^{out}_{-\mathrm{CO_2}}) + n^{lean}_{-\mathrm{CO_2}} \ln(P^{lean}_{-\mathrm{CO_2}})) \end{aligned} \tag{25}$$

In this equation, $n^i_{\mathrm{CO_2}}$ and $P^i_{\mathrm{CO_2}}$ were the molar flow rate and the partial pressure of CO_2 in the i^{th} gas stream (feed gas, lean gas, or pure outlet), while $n^i_{-\mathrm{CO_2}}$ and $P^i_{-\mathrm{CO_2}}$ represented the molar flow rate and partial pressure of all other gasses in the ith gas stream. For simplicity, we assumed a feed gas of 1 mole of total gas per unit time and a CO_2 mole fraction of 0.15, then imposed a mass balance to determine the molar flow rates of the other gas streams. For simplicity, we

assumed the total pressure of each stream ($P^i_{\mathrm{CO}_2} + P^i_{-\mathrm{CO}_2}$) was set to 1 atm, and thus had different volumetric flow rates.

The unadjusted scaling factor, w_0, was set as the quotient of the minimum work required for 90% capture divided by the minimum work to achieve the minimum lean gas partial pressure, which was the partial pressure at the final step in the reductive regeneration stage (Eq. 26). Using this ratio was particularly important for cases when $P^{lean}_{\mathrm{CO}_2} > P^{feed}_{\mathrm{CO}_2}$, which represented conditions where the pure outlet was being consumed instead of generated, because this condition typically estimated $W_{\mathrm{CO}_2} < 0$, *i.e.* energy generation from mixing of two gas streams. A scaling factor based on the minimum work of separation appropriately changed the result to be positive, preventing these conditions from appearing on the Pareto front.

$$w_0(P^{lean}_{\mathrm{CO}_2}) = \frac{W_{min}(0.1P^{feed}_{\mathrm{CO}_2})}{W_{min}(P^{lean}_{\mathrm{CO}_2})} \tag{26}$$

To obtain the complete scaling factor, we used a logistic function whose parameters were empirically tuned such that $w \approx 1$ when $P^{lean}_{\mathrm{CO}_2} < 0.1P^{feed}_{\mathrm{CO}_2}$, but $w \approx 25w_0$, its maximum value, when $P^{lean}_{\mathrm{CO}_2} > P^{feed}_{\mathrm{CO}_2}$ (Eq. 27). We set the maximum as $25w_0$ to ensure that conditions that failed to capture any CO_2 would not appear on the Pareto front, but conditions that captured some CO_2 yet did not meet the typical industry target of 90% capture ($0.1P^{feed}_{\mathrm{CO}_2} < P^{lean}_{\mathrm{CO}_2} < P^{feed}_{\mathrm{CO}_2}$) were only adjusted slightly, reflecting the US DoE's caveat that conditions that do not achieve 90% capture may still be viable if the energy consumption is sufficiently low [10].

$$w(P^{lean}_{\mathrm{CO}_2}) = \frac{25w_0(P^{lean}_{\mathrm{CO}_2})}{1 + \exp[-267(P^{lean}_{\mathrm{CO}_2} - 0.071)]} + 1 \tag{27}$$

All energies, therefore, represent the penalized energy demand of capture,

$W^*_{CO_2}$ (Eq. 28). When producing a GP surrogate model for $W^*_{CO_2}$, we fit the model to $\log_{10} W^*_{CO_2}$ because the values for $W^*_{CO_2}$ spanned multiple orders of magnitude, and fitting to untransformed $W^*_{CO_2}$ overfit to the highest energy demands, leading to overall worse accuracy.

$$W^*_{CO_2} = w(P^{lean}_{CO_2}) \frac{W_{cyc}}{\Delta DIC} \tag{28}$$

4.4. Maximum CO_2 Flux

The CO_2 flux was estimated using the van Kevelen and Hoftijzer model of gas absorption with chemical reaction enhancement [20, 56, 57, 90]. To use this model as a proxy for the total CO_2 capture rate, we assumed that the capture kinetics are limited by absorption kinetics, which has been the general consensus in the CO_2 capture literature because the homogeneous reactions related to CO_2 capture tend to be fast relative to the heterogeneous reactions [91], and the heterogeneous redox reaction at the electrode can be controlled by changing the current density and electrode area. In this model, the average CO_2 flux throughout the absorber (J) was defined as the product of: the CO_2 concentration difference between the vapor-liquid interface at the gas inlet and the bulk aqueous concentration at the liquid inlet ($[CO_2(aq)]_{V\text{-}L} - [CO_2(aq)]_\infty$); the reactor's liquid mass transfer coefficient (k_L); and a unitless enhancement factor (E), attributed to the reaction converting CO_2 into another species and increasing the effective concentration gradient at the interface. We write the equation here in terms of carbonic acid instead of the aqueous phase of CO_2 to be consistent with our chemical model (Eq. 29).

$$J = ([H_2CO_3]_{V\text{-}L} - [H_2CO_3]_\infty) k_L E \tag{29}$$

For this calculation, the concentration of H_2CO_3 in the bulk was the concen-

tration of H_2CO_3 at the end of reductive regeneration, while the concentration of H_2CO_3 at the vapor-liquid interface was at equilibrium with the assumed flue gas partial pressure (0.15 atm). We assumed a reactor mass transfer coefficient of 0.1 cm/s based on the range of typical gas absorbers reported in the literature [20]; we do not expect the selection of this constant to substantially change the solution chemistry parameters that produce optimal CO_2 capture performance because any over- or underestimation would be applied universally. The enhancement factor was calculated from the Hatta number (Ha) (Eq. 30):

$$\begin{aligned} Ha &= \frac{\sqrt{D_{\mathrm{CO_2}} k_2 [\mathrm{s}]}}{k_L} \\ E_i &= 1 + \frac{D_s[s]}{D_{\mathrm{CO_2}}[\mathrm{H_2CO_3}]_{\text{V-L}}} \\ A &= \frac{E_i - E}{E_i - 1} \\ E &= \frac{Ha\sqrt{A}}{\tanh(Ha\sqrt{A})} \end{aligned} \tag{30}$$

where $D_{\mathrm{CO_2}}$ was the diffusion coefficient of CO_2 in water (0.5*10-5cm^2/s [20]), k_2 the second order reaction rate constant of CO_2 absorption, [s] the concentration of the sorbent in the bulk solution at the start of CO_2 absorption, D_s the diffusion coefficient of the sorbent in water, and E_i the maximum enhancement factor if the reaction was instantaneous. For this calculation, we assumed the sorbent to be OH^- due to its much faster reaction rate compared to H_2O [20, 92], giving an estimated $D_s = 5.2{*}10^{-5}$ cm^2/s [93] and $k_2 = 8300$ (Ms)$^{-1}$ [20, 61, 94, 95]. Due to the rapid exchange of protons between water and hydroquinone, we assumed the concentration of sorbent in solution was better described by the sum of all proton acceptors ($[OH^-] + [QH^-] + 2[Q^{2-}]$). While this assumption of the total sorbent concentration likely led to an overestimated flux, our intention with these calculations was to estimate an idealized upper bound rate in the same way that our energy calculations were an idealized lower

bound. With this in mind, we deliberately overestimated the flux because to use only the concentration of OH^- would likely represent a slight underestimation. The calculation of the enhancement factor was simplified under specific limiting conditions according to the following rules:

$$\begin{aligned} Ha > 10E_i &: E = E_i \\ Ha < 0.5E_i &: E = \frac{Ha}{\tanh(Ha)} \\ Ha > 0.5E_i \text{ and } Ha > 3 &: E = Ha \end{aligned} \tag{31}$$

If none of these conditions were satisfied, the enhancement factor was calculated by converting Eq. 30 into a nonlinear root finding problem and solving it iteratively using a numerical Newton's method.

4.5. CO_2 Capture Constraints and Targets

The goal of the CO_2 capture model was to relate the solution chemistry properties to CO_2 capture performance, defined as the simultaneous maximization of CO_2 flux and minimization of energy demand per mole of CO_2 captured. We specifically restricted our search to the parameter space occupied by quinones, a class of molecule that undergoes a $2e^-$:$2H^+$ PCET process, due to previous theoretical [11] and experimental [23, 49] demonstrations, as well as sufficient data on the acid dissociation constants of the reduced forms of substituted quinones to restrict our search to realistic domains [87]. Quinones in this dataset whose reduction potentials were within the electrochemical window of water had $pK_{a,1}$ values in the domain of [-8.33 - 13.41] and $pK_{a,2}$ values in the domain of [-6.64 - 15.34]. Given that the lowest pH that can be achieved in solution was not likely to be much lower than the pK_a of carbonic acid (6.33), we limited both pK_a values to a minimum of 2 as a conservative constraint; all compounds with pK_a values below this should behave identically. Due to the strong correlation

between the two pK_a values (Pearson's $r = 0.875$), in order to sample only realistic combinations of pK_a values, we sampled the two equilibrium constants by selecting the pK_a of the first deprotonation event and the difference between the two pK_a values, which fell within the domain [0 - 5.5] for 99% of the dataset. While this transformation occasionally led to p$K_{a,2}$ values outside of the reported domain, we found that applying this additional restriction increased the computational cost without substantially changing the Pareto front. The total concentration of quinone was bounded between 10 mM and 3 M. The lower bound was estimated based on the lower bound concentration of redox species in previous electrochemical CO_2 capture studies [13], while the upper bound was set at 50% greater than the highest reported quinone solubility we found in the literature [23] to accommodate possible future improvements. The concentration of acid or base was capped at 15 M for practical safety should the results be implemented, and concentrations below 10 nM were assumed to be effectively 0 due to the comparatively higher concentrations of quinone.

We were specifically interested in what specific solution chemistry properties led to performance that was comparable to or better than the flux and energy demands of CO_2 capture from coal power plant flue gas (15v% CO_2) by temperature-swings using 30wt% MEA in water. Experimental measurements of state-of-the-art pilot plants estimated that the energy demand for regenerating the MEA sorbent was approximately 110 kJ of thermal energy per mole CO_2 [96]; assuming an average 35% thermal-to-electrical efficiency of a coal power plant [20, 21], this is approximately 38 kJ_e/mol C. Using the same assumptions and model as Section 4.4 and reported constants for MEA in the literature [20], we estimated the flux of CO_2 capture as 22 mmol/m^2s. Due to the relative importance of energy compared to rate in the CO_2 capture literature and the fact that our energy demand calculations do not account for any resistive losses,

we defined Competitive performance as having an energy demand lower than that of capture by the MEA process while also having a flux greater than 10% of that of the MEA process. We selected 10% of the flux as the cutoff because alternative sorbents used in industry, such as AMP, have roughly 5 to 10 times slower second order rate constants [97, 98].

We defined two additional selection criteria based on single objective optimization: Minimum energy and Maximum flux. Minimizing the energy was bounded by the same cutoff value for flux as Competitive performance, but it defined the energy demand cutoff as 22 kJ_e/mol C based on the target set by the US Department of Energy [10, 51]. Maximizing the flux searched for conditions that had a flux greater than that of the MEA benchmark with energy demands $<$45 kJ_e/mol C, the maximum energy demand on the estimated Pareto front. To obtain our adaptively sampled dataset, we first obtained an initial sample design using a coarse grid with additional random sampling ($n = 52$), searched for the Pareto front ($n = 100$), adaptively sampled for conditions that capture CO_2 in flue gas rather than release CO_2 into it ($n = 100$), adaptively sampled for the Competitive performance criteria ($n = 100$), then alternatingly adaptively sampled for Maximum flux and Minimum energy criteria ($n = 50$ each). In this study, while it was possible to conduct the contour estimations prior to Pareto front estimation, we first searched for the Pareto front to identify if any points could meet the selection criteria we defined. We conducted the search for conditions that captured CO_2 instead of releasing it after searching for the Pareto front to discern if the sample domain could be constrained to reduce the likelihood of sampling conditions that would rarely capture any CO_2. The adaptive sampling procedures were repeated for both the basic and acidic conditions separately, then the results aggregated together for analysis.

5. Application to CO_2 Capture

The sampled data from the CO_2 capture model showed a broad distribution of possible energy and flux results among different chemical property combinations (Figure 5); we have highlighted three representative points for later analysis. We note that Figure 5 only represents 48% of the samples and a fraction of the breadth of possible outcomes to maintain useful resolution: of the 904 total samples, 444 points were omitted from the figure for insufficient capture (negative flux), while 35 points were omitted for sufficient capture but prohibitive energy demand ($>$ 100 kJ_e/mol C). The range of sampled penalized energy demands was 6.6 to 10^7 kJ_e/mol C, while the range of CO_2 fluxes was -10^4 to 30 mmol/m^2s. Using a GP classifier, we estimated that a solely random solution composition has a 76% chance of capturing some CO_2 from flue gas but only a 27% chance to be competitive with the MEA benchmark with respect to both energy and rate. Using the GP as a regressor, the median penalized energy demand was 73 kJ_e/mol C, and the median CO_2 flux was 4.8 mmol/m^2s, indicating that capture would be likely, but the energy demand would be too high for practical implementation (Figure S7). We note that the median estimate for the energy demand has a large uncertainty because it is far from the high density of samples near the contours of interest. From the estimated Pareto front, it was clear that the minimum energy demand of CO_2 capture by PCET-driven pH swings can be substantially lower than that of capture by temperature-swing of MEA solutions [20, 96], and potentially lower than the DoE target [10, 51], even when accounting for reported energy efficiencies of electrochemical CO_2 capture [14, 15, 16, 17, 18, 19].

The lowest among sampled energy demands was only 6.6 kJ_e/mol C, less than half of the 16 kJ_e/mol C minimum that Jin et al. [11] calculated for the same exact system when only considering high hydroquinone pK_a values, and

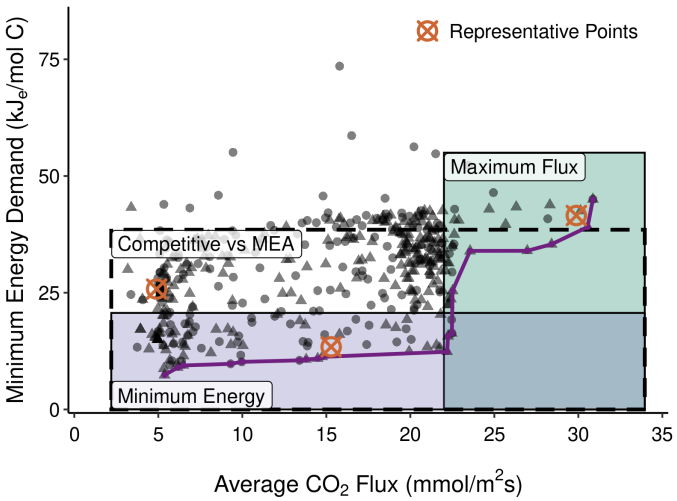

Figure 5: The performance of PCET-based pH swings for CO_2 capture due to changes in hydroquinone pK_a values, quinone concentration, and pH correction magnitude compared to the three regions of interest. Purple line is the estimated Pareto front. Representative points have been highlighted for later analysis.

this value approaches the limiting thermodynamic work of separation of 5.4 kJ_e/mol C. Given that this sample, and all samples on the Pareto front with energy demands less than 10 kJ_e/mol C, had a first pK_a less than 7 and a second pK_a less than 10, both deprotonated species should make up a substantial fraction of the hydroquinones at some point during the process. This highlights the importance of including the entire set of reactions in the chemical model, as the oft-ignored deprotonation reactions may have positive benefits like lowering the energy requirement. In this case, the lower minimum energy demand was due to the relationship between the electrode potential and the pH (Eq. 20). When the deprotonation reactions are included, the pH should be buffered, leading to smaller differences between the anode and cathode potentials and lower electrochemical work per cycle.

While the calculated energy demands were promising, few samples exceeded the flux of the MEA benchmark [20], although many were of a similar order of

magnitude. Notably, there was a sharp increase in the energy demand at nearly-constant flux at roughly the same flux as MEA. Preliminary exploratory calculations indicated that this feature was caused by two factors: limited concentrations and limited differences in the pK_a values (Figure S8). The concentration of quinone sorbent was bounded based on a literature search of quinone solubilities [11, 23, 49], and thus was capped at 3 M compared to the 30wt% MEA solutions (approximately 5 M) of the temperature-swing benchmark. Other studies in the literature showed that lower concentrations led to a lower pH at the onset of absorption and would limit the fluxes by reducing the total sorbent concentration in the enhancement factor calculation (Eq. 30) [11]; calculations with higher concentrations generally shift the Pareto front towards higher fluxes. Similarly, while we limited the difference between the two pK_a values of the hydroquinone to a maximum of 5.5 to capture 99% of the available dataset of measured hydroquinones [87], calculations that decreased the difference between the pK_a values shifted the near-vertical component of the Pareto front towards lower fluxes. Increasing the difference did not substantially change the location of the Pareto front, suggesting asymptotic behavior, but finding compounds with greater differences in their pK_a values would increase the fraction of the search domain meeting the Maximum flux criteria.

To understand what solution chemistry property combinations would produce performance with low energy demands, high capture rates, or both, we first calculated the marginals-based classifier variable importance rankings from single variable marginals (Figure 6). The Competitive performance and Minimum energy criteria had the same ranking of variables, likely because conditions meeting the Minimum energy criteria also met the Competitive performance criteria. In these two cases, the equilibrium constants were the most important, followed by the concentrations, then the decision between adding acid or base. The equi-

librium constant of the second deprotonation was more important than that of the first deprotonation reaction, which had an importance that was similar to the concentrations. When targeting higher fluxes, the quinone concentration became the most important variable, consistent with our preliminary exploratory calculations (Figure S8). Apart from this shift in importance of the quinone concentration, the Maximum flux criteria ranked the variables identically to the other criteria. These rankings were highly sensitive to the bounds that we set for each variable in our search (Section 4.5). For instance, decreasing the lower bound of the concentration could have increased its relative importance by including many points where capture was impossible, resulting in a lower average variance of other variables and increasing its importance (Eq. 7). However, the bounds that we set were based on available descriptions of real systems or data of candidate compounds, and we do not believe these findings to be biased by any desire to inflate the importance of any particular variable. In fact, by setting the lower bound of the $\mathrm{p}K_\mathrm{a}$ values at 2 instead of the lower bounds from the dataset of -8.33 and -6.64 for $\mathrm{p}K_{\mathrm{a},1}$ and $\mathrm{p}K_{\mathrm{a},2}$, respectively, we decreased the importance of the $\mathrm{p}K_\mathrm{a}$ values, yet they were still highly ranked variables, suggesting that our choices had limited impact on the ordinal rankings.

To understand why the quinone concentration was more important for high fluxes but less important for the other selection criteria, we analyzed the single variable marginals. These marginals were calculated both over the full set of other variable possibilities, X_{-i}, as well as over a subset $X^*_{-i} \in X_{-i}$ where all variables x_j more important than variable x_i were restricted to a suggested domain but all variables x_k less important than variable x_i retained their full search domain (Eq. 32). We define $P^*|x_i$ as the marginalization over this restricted subset X^*_{-i} and define the suggested domain as the set x_i values for which $P^*|x_i$ is greater than a 1:3 weighted average of the minimum and

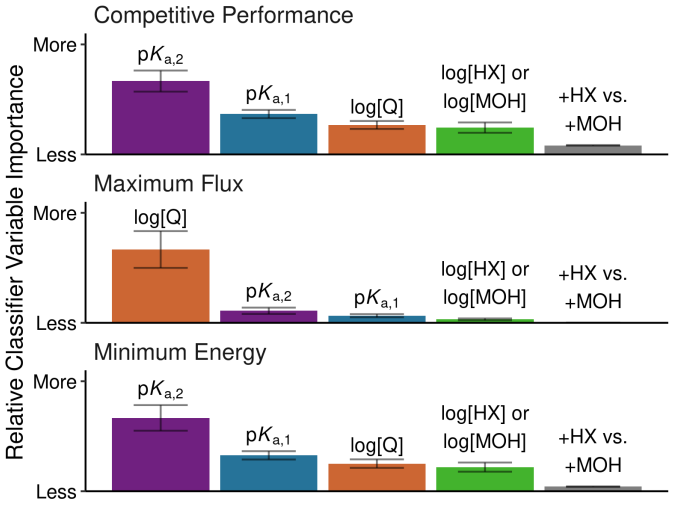

Figure 6: Importance ranking of solution composition variables for being (top) competitive with the MEA benchmark with regards to both its flux and energy demand, (middle) having a faster flux than the benchmark, or (bottom) meeting the DoE energy target. Logarithms are all base 10. [Q] = concentration of quinone. log[HX] or log[MOH] = net concentration of additional base or acid. +HX vs. +MOH = binary decision of net acid or base addition.

maximum $P^*|x_i$. By definition, for the most important variable x_n, $P^*|x_n$ is the same as $P|x_n$, leading to a sequential determination of the suggested domains for each variable in the order of their importance. We used a suggested domain rather than simply constraining to the singular optimal values of more important x_j to account for both noise in the Monte Carlo estimate of $P|x_i$ and the fact that it is unlikely that a compound exists with all the optimal properties exactly.

$$P^*|x_j^* \geq 0.25 \min(P^*|x_j) + 0.75 \max(P^*|x_j) \tag{32}$$

For the Competitive performance (Figure 7) and Minimum energy (Figure S9) criteria, the concentration of quinone had a minimum threshold value of approximately 30 mM, below which the probability of meeting the criteria was nearly 0 with a low variance, but above which the probability was nearly con-

Table 1: Suggested solution chemistry property domain (and optimum) for PCET-based pH swing CO_2 capture, from most to least important the Competitive performance criteria.

	Competitive performance	Minimum energy	Maximum flux
$pK_{a,2}$	9.12 - 11.88 (10.73)	9.12 - 11.65 (10.27)	14.64 - 19.00 (16.70)
$pK_{a,1}$	4.85 - 9.20 (4.85)	4.71 - 9.05 (4.92)	10.55 - 12.67 (12.26)
Quinone concentration	37 mM - 3.2 M (420 mM)	41 mM - 2.3 M (260 mM)	1.9 M - 3.2 M (2.9 M)
Acid or base concentration	100 nM - 21 mM (810 μM)	78 nM - 9.9 mM (710 μM)	1.4 μM - 650 mM (55 mM)

stant with a moderate variance. For the Maximum flux criteria (Figure S10), this profile was the same shape, but the threshold concentration for nonzero probability and nonzero variance increased to nearly 1 M, leading to a lower average variance and greater importance. Regardless of the selection criteria, the peak in the probability was >100 mM (Table 1), although the shape of the marginals suggests there was a negligible difference between this peak probability and that of the upper bound concentration of 3 M. Restricting the integration to only the suggested pK_a domains rather than the full pK_a domains only amplified the difference between the zero and nonzero probabilities in the way that we would expect when we exclude low likelihood pK_a values; it did not change the concentration where the probability has the step increase.

Like the quinone concentration, both pK_a marginals had a specified value below which the probability and variance were both negligible. Consistent with our hypothesis based on other pH-swing driven systems [13], both pK_a marginals showed an optimum that we believe to be the result of maximizing the use of the pH buffering capacity. However, the marginals revealed an important asymmetry to this peak, where pK_a values that were greater than this optimal value were more likely to produce desirable results than lower pK_a values. This was likely because increasing the pK_a values led to a higher maximum solution pH, but the relationship between maximum solution pH and pK_a appeared

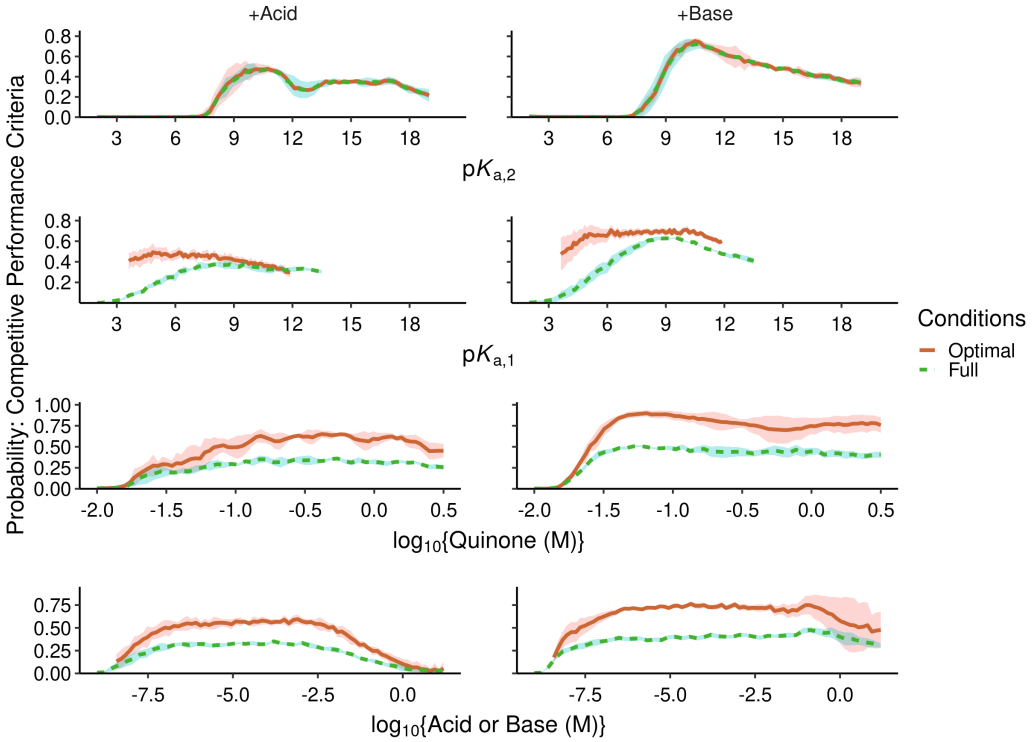

Figure 7: Single variable marginalizations of the four continuous solution chemistry properties of interest. Marginals are conditioned on the full domain of less important variables and either the full or optimal domain of the more important variables (rows are from most to least important). Shaded region is the standard error of the mean (n = 1,500).

asymptotic [11], leading to a negligible difference in performance among the highest pK_{a} values.

The importance of the relative difference between the pK_{a} values was highlighted in the change in the p$K_{\mathrm{a},1}$ marginals before and after conditioning on suggested p$K_{\mathrm{a},2}$ domain. The upper bound of the suggested domain for p$K_{\mathrm{a},2}$ was lower than the full domain by multiple pH units (Table 1), and the peak in the optimal p$K_{\mathrm{a},1}$ decreases by a similar amount when conditioning on the suggested p$K_{\mathrm{a},2}$ domain. This was most notable for the Competitive performance and Minimum energy criteria. For the Maximum flux criteria, the upper

bound of the suggested domain for $pK_{a,2}$ was higher, so restricting the $pK_{a,1}$ marginals over the suggested domain had less effect (Figure S10).

Concentrations of the additional acid or base generally show nonzero probabilities for moderate concentrations, and high or low concentrations had low likelihoods of meeting any selection criteria. The fact that the extremes of acid or base addition led to a negligible likelihood indicated that large deviations from an ideal operating pH in either direction led to worse performance. However, for the nonzero moderate concentrations, these marginals were relatively flat, indicating that this variable was forgiving compared to the other variables of interest. We note, however, that the suggested concentration for this species is often in the μM to mM range (Table 1). Combined with its position as the least important continuous variable, we interpret the amount of net acid or base as a tuning parameter for the case when trade-offs must be made among the pK_a values and solubilities during quinone selection.

Overall, the optima in the pK_a and acid or base concentration marginals indicated an optimal pH window of operation and suggested that the process is not well described as a "pH swing" process. Describing the process as being driven by pH swings suggests it would produce similar CO_2 capture performance for either the same change in pH (*e.g.*, 4 to 7 versus 7 to 10) or the same change in proton concentration (*e.g.*, 1 to 2 mM versus 4 to 5 mM). Instead, the presence of optima at intermediate values for these three variables suggested that the pH window itself is of importance, and we argue that the process is therefore better described by changing the pH buffer capacity of the system [13].

A closer look at the binary decision of whether the pH adjustment should be acidic or basic reveals a notable shortcoming to our methodology (Figure S11). This variable not only had limited quantitative impact as noted by its low importance ranking, but also the suggested domains for adding acid, base, or

randomly assigning the pH adjustment direction differed by less than 5%, allowing us to simplify our reporting of the suggested domains assuming a randomly assigned pH adjustment direction (Table 1). Qualitatively, however, there was a notable difference among adding acid or base for the Maximum flux selection criteria (Figure S10), despite its low relative importance. In other words, variables with low relative importance in the ranking could still have a noticeable impact. While we could have included an uncorrelated reference variable to determine if a variable has any quantifiable impact [99], there is no consensus of how large of a difference in the importance metric is necessary to discern whether two variables are similar in their impacts or if one is more important than the other. This, however, is a common problem among many variable importance measures, where decisions often come from user decisions of what is "good enough" [100].

This shortcoming may explain the change to the variable importance ranking when remapped onto relative variables: $\mathrm{p}K_{\mathrm{a},1}$, the $\mathrm{p}K_{\mathrm{a}}$ difference, the total quinone concentration, and the ratio of HX or MOH concentration to quinone concentration. This was the set of variables that we used during the sampling process because it removed correlations between input variables, converting the sample space to a hypercube. While our exploratory calculations suggested that the difference in the $\mathrm{p}K_{\mathrm{a}}$ values impacted the predicted flux, the importance ranking indicated that the $\mathrm{p}K_{\mathrm{a}}$ difference was lowly ranked for all selection criteria (Figure S12). As evident from the importance of the pH adjustment direction, a low ordinal ranking is not equivalent to having no impact, although its ranking less than the quinone concentration in all selection criteria suggests a decrease in the importance of at least one $\mathrm{p}K_{\mathrm{a}}$ due to this transformation of variables. At present, we are unaware of any research on how remapping or transforming variables should be standardized for consistency in variable im-

portance ranking. At a glance, we think this problem has the potential to be abused to confirm biases in a similar way to data dredging [101, 102], so we advise scrutiny when seeing and using importance rankings without transparency of assumptions and motivations. Our approach to limiting bias was to define the variables as they would be measured or reported in practice, as those are the most easily interpreted and used.

While the single variable marginals were useful in understanding how the system behaved at a macro-level, they were not helpful in understanding why the system performed better or worse under those conditions beyond speculation. To glean this information, we selected 3 specific points for a closer inspection of the entire process cycle (Figure 5): the peak predictions from the Competitive performance ("Peak prediction") and Maximum flux ("High flux") criteria (Table 1), and a point that had an intermediate energy demand but low flux ("Poor performance," $\mathrm{p}K_{\mathrm{a},1} = 4.92$, $\mathrm{p}K_{\mathrm{a},2} = 9.49$, $\{\mathrm{Q}\}_{\mathrm{tot}} = 23$ mM, $\{\mathrm{HX}\} = 6.6$ mM). These three points represented the span of low, moderate, and high energy demand and flux but combined in a way such that we could interpret effects on energy and flux separately. We specifically looked at two pairs of variables over the 4-stage cycle: (*1*) electrode potential and fraction of reduced quinone and (*2*) solution pH and total DIC (Figure 8). The area contained within the electrode potential-fraction of reduced quinone curves was proportional to the electrochemical work required per cycle, while the solution pH-DIC plots represented the driver and result of CO_2 removal from the gas phase, respectively.

The most obvious difference among these three points was in the energy consumed per cycle: the High flux prediction required the most energy per cycle, followed by Peak prediction and Poor performance examples. This order was slightly unexpected because the Poor performance example had a greater

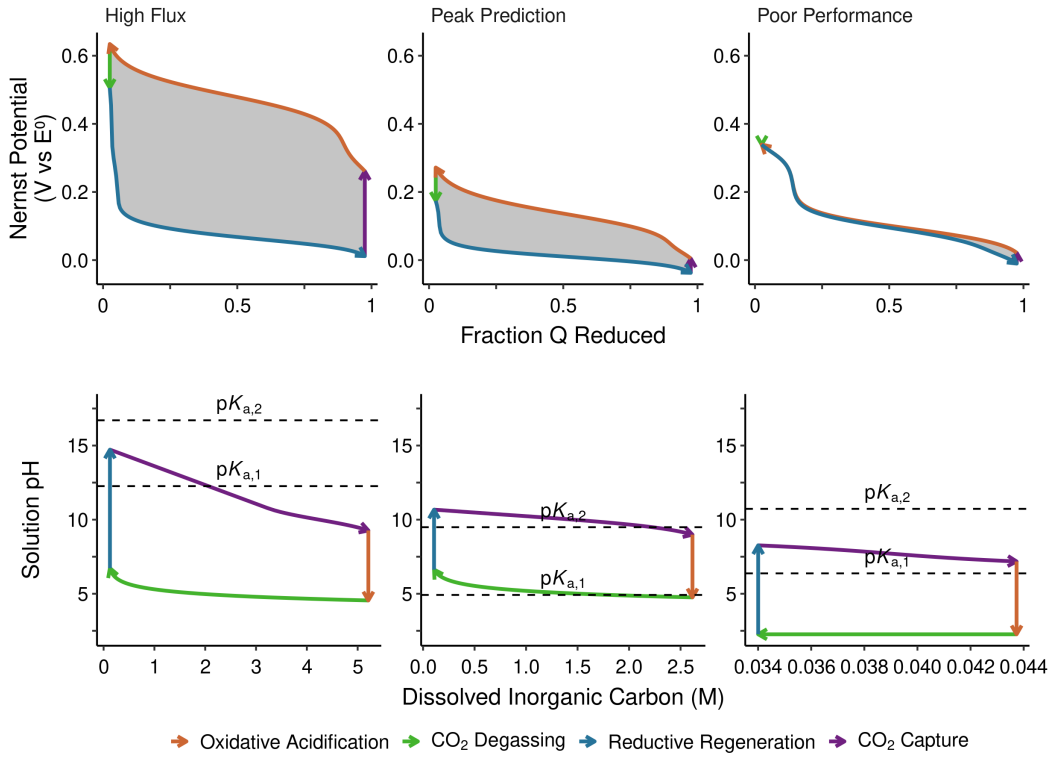

Figure 8: Process cycles of representative simulations. (top) Electrode potential changes as quinone is reduced or oxidized. (bottom) Bulk solution pH as the concentration of dissolved inorganic carbon changes. Quinone concentrations: High flux = 2.7 M; Peak performance = 51 mM; Poor performance = 23 mM.

energy demand than the Peak prediction, but this can be explained by the low CO_2 captured per cycle: the Poor performance example only captured 9 mM CO_2 per cycle compared to the 2.5 M from the Peak prediction. As a result, while the energy demand per cycle was lower for the Poor performance example, its normalized energy demand per mole of CO_2 was greater. While the High flux prediction captured even more CO_2 per cycle at approximately 5 M, it was insufficient to counteract the increase in energy demand per cycle, resulting in the highest energy demand among the three points. The small ΔDIC of the Poor performance example can be attributed to the low concentration of

quinone (23 mM).

The rationale for these energy demands per cycle can be explained using Eq. 20 and the pH changes over the course of the process. Generally, the anode and cathode potentials will be closer together, and thus the energy demand per cycle lower, if the pH of the oxidation and reduction stages are similar. Without any CO_2 changes in the system, there should be no hysteresis, but the presence or absence of acidity from carbonic acid caused the two electrode potentials to differ. Minimizing the pH change of a single half-cycle can be achieved if the pH was near the hydroquinone pK_a values and thus within the buffer regime of the hydroquinone. For the High flux point, the hydroquinone pK_a values were comparatively high, helping drive the operating pH higher and increasing the ΔDIC. While this may appear to be beneficial by reducing the number of cycles to capture the same amount of CO_2, this would also increase the acidification from CO_2 and drive the pH of the oxidation stage down. Therefore, for the High flux prediction, due to both the decrease in pH and high DIC compared to the total quinone concentration (3 M), while the reduction stage was largely buffered by the QH_2/QH^- reaction ($pK_a = 11.2$), the oxidation stage was transitions from being buffered by the HCO_3^-/CO_3^{2-} reaction ($pK_a = 10.33$) to the H_2CO_3/HCO_3^- reaction ($pK_a = 6.33$) as oxidation progressed. In contrast, the Peak prediction and Poor performance example had a much smaller decrease in pH after the CO_2 absorption stage, keeping the anode and cathode pH closer together. This rationalized our finding that there was a peak in both pK_a marginals: there is an optimal domain of pK_a values that represents the balance between having a sufficiently high pK_a to capture large quantities of CO_2, but a low enough pK_a that the pH can be buffered by hydroquinone during operation. From our perspective of pH buffering, rather than simply pH swings, it makes sense that the suggested domains of the pK_a values are roughly centered

around the pK_a values of the H_2CO_3/HCO_3^- (6.33) and HCO_3^-/CO_3^{2-} (10.33) reactions (Table 1). The similarity would mean that regardless of whether the system has high or low DIC, the dominant buffer in solution has a similar pK_a value, keeping the anode and cathode pH profiles similar regardless of DIC.

Consistent with our marginalizations, the flux was optimized by higher pK_a values and quinone concentrations, as these two variables contribute to higher OH^- concentrations and thus faster reaction rates. As previously reported in the literature [11], both higher pK_a values and higher concentrations led to higher pHs at the start of CO_2 absorption. While those authors interpreted this in the context of maximizing CO_2 capture per cycle, this will also increase the sorbent (OH^-) concentration, and thus capture rate (Eq. 30). Additionally, these variables appeared to cause to a lower minimum $P_{CO_2}^{lean}$: 10^{-13} atm for the High flux prediction compared to 10^{-5} and 10^{-2} for the Peak prediction and Poor performance example, respectively. Consequently, the concentration gradient term in Eq. 29 increased as well, leading to a slightly greater flux. However, because this term is a difference between the surface and bulk concentrations, the effect is asymptotic, so the change in sorbent concentration is necessary for a complete explanation of the increase in rate.

Having developed our understanding of the CO_2 capture model, we used the trained GP classifier to screen a substituted hydroquinone pK_a dataset for quinones that would produce a process whose performance was competitive with the MEA benchmark (Table SI) [87]. Few quinones in the dataset had reported solubilities in water, and none had published solubilities for the highly conductive, high ionic strength solutions one would use in an electrochemical process, so for this calculation, we marginalized over the limits of quinone and acid/base concentrations that we applied in our search. As a result, these probabilities are likely overestimates, and we only use them to provide insight into chemical

trends. Of the 127 compounds, 84 were more likely to be competitive with the MEA benchmark than not. We estimate that the most promising molecule, 2,3-bis(dimethylamino)-*p*-benzoquinone, could have lower energy demands and greater fluxes than the MEA benchmark in 85% of solution compositions in the search domain with its pK_a values of 9.43 and 11.11.

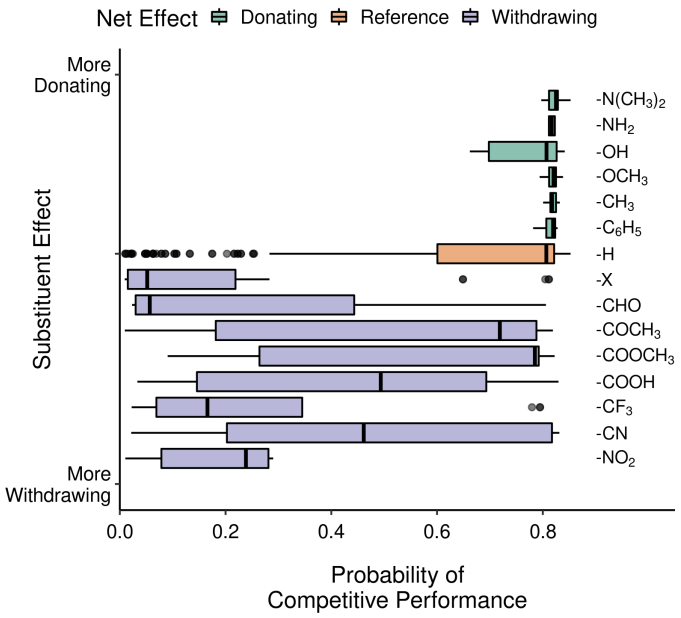

Figure 9: Application of the adaptive-sampling refined GP classifier to a dataset of substituted hydroquinone pK_a values [87]. Probabilities are after marginalization across the training domain of concentrations due to lack of solubility information.

To determine if there were any patterns related to the properties of the functional group substitutions, we labeled the probabilities with the quinone's functional groups and ranked them according to their electronic substituent effects for aromatic systems from the most electron donating to most electron withdrawing (Figure 9) [103]. As a first pass on this analysis, quinones with multiple substitutions had their probabilities included for each substitution, *e.g.*, a quinone with two halide substitutions ($-$X) and an amine ($-NH_2$) contributes twice to the dataset of halides and once to the dataset of amines.

In general, ~~functional groups that were more electron donating had higher probabilities of being competitive with the MEA benchmark. We believe this was~~ electron donating groups almost always predicted low energy-high rate CO_2 capture performance, whereas electron withdrawing groups had a wide variance in their likelihood of predicting both low energy demands and high capture rates. This trend occurred because electron donating groups ~~will increase the~~ tend to increase the pK_a values by increasing the electron density around the oxygen atoms~~of the hydroquinone, thereby increasing the attraction of the oxygen atom to the proton, which would increase the~~ , whereas electron withdrawing groups do the opposite. Given that the single variable marginalization for both pKa values look roughly like step functions with an overshoot at the step (Figure 7), variation in the strength and number of electron donating groups, and thus variation in its impact on the magnitude of the pK_a increase, was not likely to show much variance in the probability, particularly because the unsubstituted *p*-benzoquinone has pK_a values close to the optimum (9.85 and 11.4). However, variation in the strength and number of the electron withdrawing groups~~were not necessarily a detriment, as there were compounds with electron withdrawing groups that had high probabilities ($>$ 0.80) of being competitive with the MEA benchmark, as did unsubstituted *p*-benzoquinone. Additionally, electron withdrawing groups were found to increase the reduction potentials of the quinones (Figure S13), and thus these quinones would be more resistant to oxidation in the presence of O_2 gas, a factor that we did not include in the CO_2 capture model. A third objective function relating standard reduction potential to stability would need to be included in order to discern how, if at all, stability would affect the selection of the sorbent molecule~~, and thus the magnitude of a pK_a value decrease, would cause large variations in the likelihood of meeting both the energy and rate criteria, as it would span from

this baseline probability near the peak down to zero. The lack of a clear trend with the magnitude of the substituent effect, where stronger withdrawing groups in particular still showed high probabilities, was largely because we only looked at single-substituent effects, and thus do not include concerted or conflicting effects of multiple substituent groups.

While the dataset could be analyzed beyond single substitution effects, we did not conduct further analyses because our conclusions were substantially biased by the small dataset size. For instance, a preliminary analysis of the number of substitutions indicated that as the number of substitutions increased, the median probability of acceptance decreased, but there were approximately three times as many compounds in the dataset with two substitutions than compounds with any other number of substitutions. As a result, the median probabilities of mono-, tri-, or tetra-substituted compounds could have been artificially skewed by the selection of candidates in the dataset and may not have been a true reflection of the effect of the number of substitutions. We also caution using the list of compounds (Table S1) as a definitive ranking of feasibility due to the lack of solubility data in concentrated electrolytes, which would substantially alter these probabilities if the solubility limit is close to the threshold for CO_2 capture. With ~~a wider set of candidate compounds and dataon solubility in concentrated electrolyte solutions~~additional data, we would be able to make more concrete suggestions for solution compositions that could be competitive with capture by temperature-swings of MEA solutions. These data could include, for instance, the measurements of key properties, e.g. stability to common oxidants and solution viscosity, as well as the inclusion of data on compounds with solubility-enhancing substituent groups [104]. We expect stability considerations, for instance, to have a large impact on our analysis given that electron donating groups lead to more favorable pK_a values but

also lower reduction potentials (Figure S13), and thus should be less stable in the presence of O_2. A third objective function relating standard reduction potential to stability would need to be included in order to discern how, if at all, stability would affect the selection of the sorbent molecule. The power of the multiobjective approach described in this work is that it can accommodate these additional objective functions by considering all objectives simultaneously, preventing any overcorrection caused by a single objective and describing where and how trade-offs among objectives arise.

6. Broader Implications

This paper provided foundational work in two areas: (*1*) experiment designs for supervised classifier refinement and (*2*) CO_2 capture driven by PCET reactions. In the context of refining a supervised classifier, our work described a new adaptive sampling method that can improve binary classification based on a continuous output and a predefined threshold by sampling points that will improve the precision of the boundary between the two classes. The sampling process accomplished this by prioritizing points that had both a small distance to the contour of interest and a high uncertainty in that estimate, balancing exploitation of known information with exploration of under-sampled regions of the domain. Importantly, our approach was generalized to be able to handle classification definitions based on multiple overlapping criteria, which often leads to a piecewise contour. This can be applied to numerous engineering problems where there are specific targets, such as designing for reliability, satisfying design constraints, or maintaining regulatory compliance [28, 29, 30, 31, 32, 45, 46, 47, 105]. In addition, we developed a framework for interpreting the classifier to assist engineering design by suggesting conditions that will achieve those targets with the greatest estimated probability. In case the suggested conditions cannot be

achieved due to trade-offs between specific variables, we also developed a metric for comparing the relative importance of each variable to indicate which should be prioritized in the trade-off.

In the context of CO_2 capture driven by PCET electrochemical reactions, we identified that the hydroquinone pK_a values are the most important variables to consider when selecting a compound to have CO_2 capture performance competitive with the MEA benchmark. While quinone concentration, and by proxy the quinone solubility limit, was important, the concentration must only be at least 50 mM to be comparable to the MEA benchmark in terms of both energy demand and CO_2 capture rate; a high concentration is only necessary if seeking to design a process with higher CO_2 capture rates than the MEA benchmark. The optima in the pK_a marginals suggested that the conceptual mechanistic model of CO_2 capture should be framed in terms of changing the pH buffer capacity of the solution by transformation between the buffering hydroquinone and non-buffering quinone forms rather than simply framing the mechanism as a change in pH or proton concentration. This interpretation properly accounts for how to balance the amount of CO_2 captured per cycle and the energy demand per cycle, which are both highly dependent on the exact operating pH window, in order to minimize the energy per mole of CO_2 captured. While we constrained our training dataset and search domain based on existing data on substituted *p*-benzoquinones, the suggested equilibrium constants and concentrations that we found in this study are likely to be applicable to other compounds that undergo a 2-electron, 2-proton PCET reaction such as naphthoquinones, anthroquinones, and some flavins. When we applied our model to reported pK_a data of substituted *p*-benzoquinones, we found that electron donating groups make the molecule more likely to perform competitively with the MEA benchmark in both energy demand and capture rate, although the

presence of an electron withdrawing group was not necessarily detrimental.

Beyond just PCET-based pH swings, this framework for analyzing an electrochemical CO_2 capture process could be applied to other electrochemical CO_2 capture mechanisms such as the EMAR process ~~[55]~~[55, 106, 107], ion selective membrane-based separations [22, 50, 51], or redox state-dependent sorbents [52, 53, 54]. Doing so would not only optimize those solution compositions, but it will also provide a means of comparing the thermodynamics and kinetics of the different electrochemical approaches based on their fundamental limits rather than trying to compare them based on potentially incomparable experiment designs. This would give engineers an indication of which specific electrochemical approach would be best for their application and potentially accelerate electrochemical CO_2 capture's implementation into the market, ultimately helping curb the effects of climate change.

CRediT authorship contribution statement

J.B.: Conceptualization, Methodology, Software, Validation, Formal analysis, Investigation, Data curation, Writing - Original draft. **K.P.**: Writing - Review & editing. **C.G.**: Conceptualization, Supervision, Project administration, Funding acquisition, Writing - Review & editing.

Declaration of Competing Interest

The authors have no known financial interests or personal relationships that influenced the work of this paper.

Acknowledgements

This work was supported by the US National Science Foundation [grant number NSF-CBET 1749207].

Data Statement

All codes used in generating the data for this paper are available through github (https://github.com/jkboualavong/MultiObjAdaptSamp) after publication. This repository includes additional calculations of other simpler test scenarios and some preliminary calculations not included in this paper.

References

[1] T. Stocker, D. Qin, G.-K. Plattner, M. Tignor, S. Allen, J. Boschung, A. Nauels, Y. Xia, V. Bex, P. Midgley (Eds.), Climate Change: The Physical Science Basis. Contribution of Working Group I to the Fifth Assessment Report of the IPCC, Cambridge University Press, Cambridge, United Kingdom and New York, NY, USA, 2013.

[2] O. Hoegh-Guldberg, D. Jacob, M. Taylor, M. Bindi, S. Brown, I. Camilloni, A. Diedhiou, R. Djalante, K. Ebi, F. Engelbrecht, J. Guiot, Y. Hijioka, S. Mehrotra, A. Payne, S. I. Seneviratne, A. Thomas, R. Warren, G. Zhou, Impacts of 1.5^{o}C global warming on natural and human systems, in: V. Masson-Delmotte, P. Zhai, H. O. Pörtner, D. Roberts, J. Skea, P. Shukla, A. Pirani, W. Moufouma-Okia, C. Péan, R. Pidcock, S. Connors, J. B. R. Matthews, Y. Chen, X. Zhou, M. I. Gomis, E. Lonnoy, T. Maycock, M. Tignor, T. Waterfield (Eds.), Global Warming of 1.5°C. An IPCC Special Report, International Panel on Climate Change, 2018.

[3] E. Kriegler, G. Luderer, N. Bauer, L. Baumstark, S. Fujimori, A. Popp, J. Rogelj, J. Strefer, D. P. Van Vuuren, Pathways limiting warming to 1.5°C: A tale of turning around in no time?, Philosophical Transactions of the Royal Society A: Mathematical, Physical and Engineering Sciences 376 (2119) (2018). doi:10.1098/rsta.2016.0457.

[4] National Academies of Sciences Engineering and Medicine, Negative Emissions Technologies and Reliable Sequestration, National Academies Press, 2019. doi:10.17226/25259.

[5] D. W. Keith, G. Holmes, D. St. Angelo, K. Heidel, A Process for Capturing CO_2 from the Atmosphere, Joule 2 (8) (2018) 1573–1594. doi:10.1016/j.joule.2018.05.006.

[6] Global CCS Institute, Global Status of CCS 2020, Tech. rep. (2020). URL https://www.globalccsinstitute.com/resources/global-status-report/

[7] F. A. Tobiesen, H. F. Svendsen, K. A. Hoff, Desorber Energy Consumption Amine Based Absorption Plants, International Journal of Green Energy 2 (2) (2005) 201–215. doi:10.1081/ge-200058981.

[8] M. Zhao, A. I. Minett, A. T. Harris, A review of techno-economic models for the retrofitting of conventional pulverised-coal power plants for post-combustion capture (PCC) of CO_2, Energy and Environmental Science 6 (1) (2013) 25–40. doi:10.1039/c2ee22890d.

[9] P. Markewitz, W. Kuckshinrichs, W. Leitner, J. Linssen, P. Zapp, R. Bongartz, A. Schreiber, T. E. Müller, Worldwide innovations in the development of carbon capture technologies and the utilization of CO_2, Energy and Environmental Science 5 (2012) 7281–7305. doi:10.1039/c2ee03403d.

[10] M. Matuszewski, J. Ciferno, J. J. Marano, S. Chen, Research and Development Goals for CO_2 Capture Technology, Tech. rep., Department of Energy (2011).

[11] S. Jin, M. Wu, R. G. Gordon, M. J. Aziz, D. G. Kwabi, pH swing cycle for CO_2 capture electrochemically driven through proton-coupled electron transfer, Energy and Environmental Science 13 (10) (2020) 3706–3722. doi:10.1039/d0ee01834a.

[12] R. A. Shaw, T. A. Hatton, Electrochemical CO_2 capture thermodynamics, International Journal of Greenhouse Gas Control 95 (2020) 102878. doi:10.1016/j.ijggc.2019.102878.

[13] J. Boualavong, C. A. Gorski, Electrochemically Mediated CO_2 Capture Using Aqueous Cu(II)/Cu(I) Imidazole Complexes , ACS ES&T Engineering 1 (7) (2021) 1084–1093. doi:10.1021/acsestengg.1c00068.

[14] P. Millet, Unitized Regenerative Systems, Wiley-VCH, 2015. doi:10.1002/9783527676507.ch5.

[15] B. Gurkan, F. Simeon, T. A. Hatton, Quinone Reduction in Ionic Liquids for Electrochemical CO_2 Separation, ACS Sustainable Chemistry and Engineering 3 (7) (2015) 1394–1405. doi:10.1021/acssuschemeng.5b00116.

[16] L. Legrand, O. Schaetzle, R. C. De Kler, H. V. Hamelers, Solvent-Free CO_2 Capture Using Membrane Capacitive Deionization, Environmental Science and Technology 52 (16) (2018) 9478–9485. doi:10.1021/acs.est.8b00980.

[17] M. Wang, S. Hariharan, R. A. Shaw, T. A. Hatton, Energetics of electrochemically mediated amine regeneration process for flue gas CO_2 capture, International Journal of Greenhouse Gas Control 82 (December 2018) (2019) 48–58. doi:10.1016/j.ijggc.2018.12.028.

[18] M. Rahimi, K. M. Diederichsen, N. Ozbek, M. Wang, W. Choi, T. A. Hatton, An Electrochemically Mediated Amine Regeneration Process with a

Mixed Absorbent for Postcombustion CO_2 Capture, Environmental Science and Technology 54 (14) (2020) 8999–9007. doi:10.1021/acs.est.0c02595.

[19] M. Rahimi, F. Zucchelli, M. Puccini, T. Alan Hatton, Improved CO_2 Capture Performance of Electrochemically Mediated Amine Regeneration Processes with Ionic Surfactant Additives, ACS Applied Energy Materials 3 (2020) 10823–10830. doi:10.1021/acsaem.0c01859.

[20] J. Wilcox, Carbon capture, Springer New York, 2012. doi:10.1007/978-1-4614-2215-0.

[21] K. Li, W. Leigh, P. Feron, H. Yu, M. Tade, Systematic study of aqueous monoethanolamine (MEA)-based CO_2 capture process: Techno-economic assessment of the MEA process and its improvements, Applied Energy 165 (2016) 648–659. doi:10.1016/j.apenergy.2015.12.109.

[22] M. D. Eisaman, L. Alvarado, D. Larner, P. Wang, B. Garg, K. A. Littau, CO_2 separation using bipolar membrane electrodialysis, Energy and Environmental Science 4 (4) (2011) 1319–1328. doi:10.1039/c0ee00303d.

[23] C. Huang, C. Liu, K. Wu, H. Yue, S. Tang, H. Lu, B. Liang, CO_2 Capture from Flue Gas Using an Electrochemically Reversible Hydroquinone/Quinone Solution, Energy and Fuels 33 (4) (2019) 3380–3389. doi:10.1021/acs.energyfuels.8b04419.

[24] G. X. Liu, Y. S. Yu, Y. T. Hong, Z. X. Zhang, J. J. Wei, G. G. Wang, Identifying electrochemical effects in a thermal-electrochemical co-driven system for CO_2 capture, Physical Chemistry Chemical Physics 19 (20) (2017) 13230–13244. doi:10.1039/c7cp01035d.

[25] K. Z. House, A. C. Baclig, M. Ranjan, E. A. Van Nierop, J. Wilcox, H. J. Herzog, Economic and energetic analysis of capturing CO_2 from ambient air, PNAS 108 (51) (2011) 20428–20433. doi:10.1073/pnas.1012253108.

[26] S. E. Renfrew, D. E. Starr, P. Strasser, Electrochemical approaches toward CO_2 capture and concentration, ACS Catalysis 10 (2020) 13058–13074. doi:10.1021/acscatal.0c03639.

[27] R. Sharifian, R. M. Wagterveld, I. A. Digdaya, C. Xiang, D. A. Vermaas, Electrochemical carbon dioxide capture to close the carbon cycle, Energy and Environmental Science 14 (2) (2021) 781–814. doi:10.1039/d0ee03382k.

[28] R. Gharari, N. Poursalehi, M. Abbasi, M. Aghaie, Implementation of Strength Pareto Evolutionary Algorithm II in the Multiobjective Burnable Poison Placement Optimization of KWU Pressurized Water Reactor, Nuclear Engineering and Technology 48 (5) (2016) 1126–1139. doi:10.1016/j.net.2016.04.004.

[29] Y. Yang, J. Wu, Q. Luo, T. Zhang, J. Wu, J. Wang, Effects of Stochastic Simulations on Multiobjective Optimization of Groundwater Remediation Design under Uncertainty, Journal of Hydrologic Engineering 22 (8) (2017) 04017015. doi:10.1061/(asce)he.1943-5584.0001510.

[30] A. Singh, B. S. Minsker, Uncertainty-based multiobjective optimization of groundwater remediation design, Water Resources Research 44 (2) (2008) W02404. doi:10.1029/2005WR004436.

[31] A. Mantoglou, G. Kourakos, Optimal groundwater remediation under uncertainty using multi-objective optimization, Water Resources Management 21 (5) (2007) 835–847. doi:10.1007/s11269-006-9109-0.

[32] J. Bect, D. Ginsbourger, L. Li, V. Picheny, E. Vazquez, Sequential design of computer experiments for the estimation of a probability of failure, Statistics and Computing 22 (3) (2012) 773–793. arXiv:arXiv:1009.5177v2, doi:10.1007/s11222-011-9241-4.

[33] V. Picheny, Multiobjective optimization using Gaussian process emulators via stepwise uncertainty reduction, Statistics and Computing 25 (6) (2015) 1265–1280. arXiv:1310.0732, doi:10.1007/s11222-014-9477-x.

[34] R. T. Marler, J. S. Arora, The weighted sum method for multi-objective optimization: New insights, Structural and Multidisciplinary Optimization 41 (6) (2010) 853–862. doi:10.1007/s00158-009-0460-7.

[35] I. Das, J. E. Dennis, Normal-boundary intersection: A new method for generating the Pareto surface in nonlinear multicriteria optimization problems, SIAM Journal on Optimization 8 (3) (1998) 631–657. doi:10.1137/S1052623496307510.

[36] I. Y. Kim, O. L. De Weck, Adaptive weighted sum method for multiobjective optimization: A new method for Pareto front generation, Structural and Multidisciplinary Optimization 31 (2) (2006) 105–116. doi:10.1007/s00158-005-0557-6.

[37] A. Messac, A. Ismail-Yahaya, C. A. Mattson, The normalized normal constraint method for generating the Pareto frontier, Structural and Multidisciplinary Optimization 25 (2) (2003) 86–98. doi:10.1007/s00158-002-0276-1.

[38] E. Zitzler, K. Deb, L. Thiele, Comparison of multiobjective evolutionary algorithms: empirical results., Evolutionary computation 8 (2) (2000) 173–195. doi:10.1162/106365600568202.

[39] D. J. Russo, B. Van Roy, A. Kazerouni, I. Osband, Z. Wen, A tutorial on Thompson sampling, Vol. 11, 2018. arXiv:1707.02038, doi:10.1561/2200000070.

[40] A. Seko, A. Togo, H. Hayashi, K. Tsuda, L. Chaput, I. Tanaka, Prediction of Low-Thermal-Conductivity Compounds with First-Principles Anharmonic Lattice-Dynamics Calculations and Bayesian Optimization, Physical Review Letters 115 (20) (2015) 205901. arXiv:1506.06439, doi:10.1103/PhysRevLett.115.205901.

[41] S. Ju, T. Shiga, L. Feng, Z. Hou, K. Tsuda, J. Shiomi, Designing nanostructures for phonon transport via Bayesian optimization, Physical Review X 7 (2) (2017) 021024. doi:10.1103/PhysRevX.7.021024.

[42] D. M. Negoescu, P. I. Frazier, W. B. Powell, The knowledge-gradient algorithm for sequencing experiments in drug discovery, INFORMS Journal on Computing 23 (3) (2011) 346–363. doi:10.1287/ijoc.1100.0417.

[43] S. M. Moosavi, A. Nandy, K. M. Jablonka, D. Ongari, J. P. Janet, P. G. Boyd, Y. Lee, B. Smit, H. J. Kulik, Understanding the diversity of the metal-organic framework ecosystem, Nature Communications 11 (1) (2020) 1–10. doi:10.1038/s41467-020-17755-8.

[44] R. B. Gramacy, M. Ludkovski, Sequential design for optimal stopping problems, SIAM Journal on Financial Mathematics 6 (1) (2015) 748–775. arXiv:1309.3832, doi:10.1137/140980089.

[45] H. Arenbeck, S. Missoum, A. Basudha, P. Nikravesh, Reliability-based optimal design and tolerancing for multibody systems using explicit design space decomposition, Journal of Mechanical Design, Transactions of the ASME 132 (2) (2010) 0210101–02101011. doi:10.1115/1.4000760.

[46] P. Ranjan, D. Bingham, G. Michailidis, Sequential experiment design for contour estimation from complex computer codes, Technometrics 50 (4) (2008) 527–541. doi:10.1198/004017008000000541.

[47] B. J. Bichon, M. S. Eldred, L. P. Swiler, S. Mahadevan, J. M. McFarland, Efficient global reliability analysis for nonlinear implicit performance functions, AIAA Journal 46 (10) (2008) 2459–2468. doi:10.2514/1.34321.

[48] V. Picheny, D. Ginsbourger, O. Roustant, R. T. Haftka, N. H. Kim, Adaptive designs of experiments for accurate approximation of a target region, Journal of Mechanical Design, Transactions of the ASME 132 (7) (2010) 0710081–0710089. doi:10.1115/1.4001873.

[49] J. D. Watkins, N. S. Siefert, X. Zhou, C. R. Myers, J. R. Kitchin, D. P. Hopkinson, H. B. Nulwala, Redox-Mediated Separation of Carbon Dioxide from Flue Gas, Energy and Fuels 29 (11) (2015) 7508–7515. doi:10.1021/acs.energyfuels.5b01807.

[50] H. Bae, J. S. Park, S. T. Senthilkumar, S. M. Hwang, Y. Kim, Hybrid seawater desalination-carbon capture using modified seawater battery system, Journal of Power Sources 410-411 (July 2018) (2019) 99–105. doi:10.1016/j.jpowsour.2018.11.009.

[51] S. Datta, M. P. Henry, Y. J. Lin, A. T. Fracaro, C. S. Millard, S. W. Snyder, R. L. Stiles, J. Shah, J. Yuan, L. Wesoloski, R. W. Dorner, W. M. Carlson, Electrochemical CO_2 capture using resin-wafer electrodeionization, Industrial and Engineering Chemistry Research 52 (2013) 15177–15186. doi:10.1021/ie402538d.

[52] A. M. Appel, R. Newell, D. L. Dubois, M. R. Dubois, Concentration of carbon dioxide by electrochemically modulated complexation with a binuclear copper complex, Inorganic Chemistry 44 (9) (2005) 3046–3056. doi:10.1021/ic050023k.

[53] R. Newell, A. Appel, D. L. DuBois, M. R. DuBois, Studies of bicarbonate binding by dinuclear and mononuclear Ni(II) complexes, Inorganic Chemistry 44 (2) (2005) 365–373. doi:10.1021/ic049202c.

[54] R. Ranjan, J. Olson, P. Singh, E. D. Lorance, D. A. Buttry, I. R. Gould, Reversible Electrochemical Trapping of Carbon Dioxide Using 4,4'-Bipyridine That Does Not Require Thermal Activation, Journal of Physical Chemistry Letters 6 (24) (2015) 4943–4946. doi:10.1021/acs.jpclett.5b02220.

[55] M. C. Stern, F. Simeon, H. Herzog, T. A. Hatton, Post-combustion carbon dioxide capture using electrochemically mediated amine regeneration, Energy and Environmental Science 6 (8) (2013) 2505–2517. doi:10.1039/c3ee41165f.

[56] G. Astarita, Regimes of Mass Transfer With Chemical Reaction, Industrial & Engineering Chemistry 58 (8) (1966) 18–26. doi:10.1021/ie50680a006.

[57] D. W. van Krevelen, P. J. Hoftijzer, Kinetics of gas-liquid reactions part I. General theory, Recueil des Travaux Chimiques des Pays-Bas 67 (7) (1948) 563–586. doi:10.1002/recl.19480670708.

[58] M. Kim, H. J. Song, M. G. Lee, H. Y. Jo, J. W. Park, Kinetics and steric hindrance effects of carbon dioxide absorption into aqueous potassium alaninate solutions, Industrial and Engineering Chemistry Research 51 (6) (2012) 2570–2577. doi:10.1021/ie201609b.

[59] J. van Holst, G. F. Versteeg, D. W. Brilman, J. A. Hogendoorn, Kinetic study of CO_2 with various amino acid salts in aqueous solution, Chemical Engineering Science 64 (2009) 59–68. doi:10.1016/j.ces.2008.09.015.

[60] X. Q. Xiao, K. Li, On the Use of an Electrochemical Membrane Module for Removal of CO_2 from a Breathing Gas Mixture, Transactions of the Institution of Chemical Engineers 75 (1997) 438–446. doi:10.1205/026387697523903.

[61] F. Zeman, Energy and material balance of CO_2 capture from ambient air, Environmental Science and Technology 41 (2007) 7558–7563. doi:10.1021/es070874m.

[62] S. Bishnoi, G. T. Rochelle, Absorption of carbon dioxide into aqueous piperazine: Reaction kinetics, mass transfer and solubility, Chemical Engineering Science 55 (22) (2000) 5531–5543. doi:10.1016/S0009-2509(00)00182-2.

[63] J. H. Friedman, Greedy function approximation: A gradient boosting machine, Annals of Statistics 29 (5) (2001) 1189–1232. doi:10.1214/aos/1013203451.

[64] Q. Zhao, T. Hastie, Causal Interpretations of Black-Box Models, Journal of Business & Economic Statistics 39 (1) (2019) 272–281. doi:10.1080/07350015.2019.1624293.

[65] L. S. Shapley, A Value for N-Person Games, RAND Corporation, Santa Monica, CA, USA, 1952. doi:10.7249/p0295.

[66] E. Strumbelj, I. Kononenko, Explaining prediction models and individual predictions with feature contributions, Knowledge and Information Systems 41 (3) (2014) 647–665. doi:10.1007/s10115-013-0679-x.

[67] I. Sobol, Global Sensitivity indices for nonlinear mathematical models and their Monte Carlo estimates, Mathematics and Computers in Simulations 55 (2001) 271–280. doi:10.1016/S0378-4754(00)00270-6.

[68] M. Binois, V. Picheny, Gpareto: An r package for gaussian-process-based multi-objective optimization and analysis, Journal of Statistical Software 89 (8) (2019). doi:10.18637/jss.v089.i08.

[69] M. A. Bezerra, R. E. Santelli, E. P. Oliveira, L. S. Villar, L. A. Escaleira, Response surface methodology (RSM) as a tool for optimization in analytical chemistry, Talanta 76 (5) (2008) 965–977. doi:10.1016/j.talanta.2008.05.019.

[70] H. Akçay, A. S. Anagün, Multiresponse optimization application on a manufacturing factory, Mathematical and Computational Applications 18 (3) (2013) 531–538. doi:10.3390/mca18030531.

[71] D. Abooali, R. Soleimani, A. Rezaei-Yazdi, Modeling CO_2 absorption in aqueous solutions of DEA, MDEA, and DEA + MDEA based on intelligent methods, Separation Science and Technology (Philadelphia) 55 (4) (2020) 697–707. doi:10.1080/01496395.2019.1575415.

[72] K. T. Butler, D. W. Davies, H. Cartwright, O. Isayev, A. Walsh, Machine learning for molecular and materials science, Nature 559 (7715) (2018) 547–555. doi:10.1038/s41586-018-0337-2.

[73] P. I. Frazier, A tutorial on bayesian optimization (2018) 1–22arXiv:1807.02811.

[74] C. E. Rasmussen, C. K. I. Williams, Gaussian Processes for Machine Learning, MIT Press, 2006.

[75] P. I. Frazier, J. Wang, Bayesian optimization for materials design, in: Information Science for Materials Discovery and Design, Vol. 225, Springer Series in Materials Science, 2016, pp. 45–75. arXiv:1506.01349, doi:10.1007/978-3-319-23871-5_3.

[76] O. Roustant, D. Ginsbourger, Y. Deville, DiceKriging, DiceOptim: Two R Packages for the Analysis of Computer Experiments by Kriging-Based Metamodeling and Optimization, Journal of Statistical Software 51 (1) (2012) 1–55. doi:10.18637/jss.v051.i01.

[77] F. Pedregosa, G. Varoquaux, A. Gramfort, V. Michel, B. Thirion, O. Grisel, M. Blondel, P. Prettenhofer, R. Weiss, V. Dubourg, J. Vanderplas, A. Passos, D. Cournapeau, M. Brucher, M. Perrot, E. Duchesnay, Scikit-learn: Machine Learning in Python, Journal of Machine Learning Research 12 (85) (2011) 2825–2830. doi:10.5555/1953048.2078195.

[78] T. Wada, H. Hino, Bayesian Optimization for Multi-objective Optimization and Multi-point Search (2019). arXiv:1905.02370, doi:10.48550/arXiv.1905.02370.

[79] M. King, N. Mody, Numerical and Statistical Methods for Bioengineering, Cambridge University Press, Cambridge, UK, 2010.

[80] P. M. Attia, A. Grover, N. Jin, K. A. Severson, T. M. Markov, Y. H. Liao, M. H. Chen, B. Cheong, N. Perkins, Z. Yang, P. K. Herring, M. Aykol, S. J. Harris, R. D. Braatz, S. Ermon, W. C. Chueh, Closed-loop optimization of fast-charging protocols for batteries with machine learning, Nature 578 (7795) (2020) 397–402. doi:10.1038/s41586-020-1994-5.

[81] M. W. Hoffman, B. Shahriari, N. De Freitas, On correlation and budget constraints in model-based bandit optimization with application to automatic machine learning, in: Proceedings of the 17th International Conference on Artificial Intelligence and Statistics, Vol. 33, 2014, pp. 365–374.

[82] A. Lewis, S. Mostaghim, M. Randall, Evolutionary population dynamics and multi-objective optimisation problems, in: L. T. Bui, S. Alam (Eds.), Multi-Objective Optimization in Computational Intelligence: Theory and Practice, 1st Edition, IGI Global, 2008, pp. 185–206. doi:10.4018/978-1-59904-498-9.ch007.

[83] R. de S. Motta, S. M. Afonso, P. R. Lyra, A modified NBI and NC method for the solution of N-multiobjective optimization problems, Structural and Multidisciplinary Optimization 46 (2) (2012) 239–259. doi:10.1007/s00158-011-0729-5.

[84] T. C. Simpson, R. R. Durand, Reactivity of carbon dioxide with quinones, Electrochimica Acta 35 (9) (1990) 1399–1403. doi:10.1016/0013-4686(90)85012-C.

[85] Y. Liu, H. Z. Ye, K. M. Diederichsen, T. Van Voorhis, T. A. Hatton, Electrochemically mediated carbon dioxide separation with quinone chemistry in salt-concentrated aqueous media, Nature Communications 11 (1) (2020) 1–12. doi:10.1038/s41467-020-16150-7.

[86] P. Scovazzo, J. Poshusta, D. DuBois, C. Koval, R. Noble, Electrochemical Separation and Concentration of <1% Carbon Dioxide from Nitrogen, Journal of The Electrochemical Society 150 (5) (2003) D91. doi:10.1149/1.1566962.

[87] M. T. Huynh, C. W. Anson, A. C. Cavell, S. S. Stahl, S. Hammes-Schiffer, Quinone 1 e^- and 2 e^-/2 H^+ Reduction Potentials: Identification and Analysis of Deviations from Systematic Scaling Relationships, Journal of the American Chemical Society 138 (49) (2016) 15903–15910. doi:10.1021/jacs.6b05797.

[88] G. Puxty, M. Maeder, A simple chemical model to represent CO_2-amine-H_2O vapour-liquid-equilibria, International Journal of Greenhouse Gas Control 17 (2013) 215–224. doi:10.1016/j.ijggc.2013.05.016.

[89] M. A. Jenkins, J. F. Traub, Algorithm 419: Zeros of a Complex Polynomial [C2], Communications of the Association for Computing Machinery 15 (2) (1972) 97–99.

[90] B. Dutcher, M. Fan, A. G. Russell, Amine-based CO_2 capture technology development from the beginning of 2013-A review, ACS Applied Materials and Interfaces 7 (4) (2015) 2137–2148. doi:10.1021/am507465f.

[91] M. Caplow, Kinetics of Carbamate Formation and Breakdown, Journal of the American Chemical Society 90 (24) (1968) 6795–6803. doi:10.1021/ja01026a041.

[92] N. McCann, D. Phan, X. Wang, W. Conway, R. Burns, M. Attalla, G. Puxty, M. Maeder, Kinetics and mechanism of carbamate formation from CO_2(aq), carbonate species, and monoethanolamine in aqueous solution, Journal of Physical Chemistry A 113 (17) (2009) 5022–5029. doi:10.1021/jp810564z.

[93] S. N. Lvov, Introduction to Electrochemical Science and Engineering, CRC Press, 2012.

[94] Y. Pocker, D. W. Bjorkquist, Stopped-Flow Studies of Carbon Dioxide Hydration and Bicarbonate Dehydration in H_2O and D_2O. Acid-Base and Metal Ion Catalysis, Journal of the American Chemical Society 99 (20) (1977) 6537–6543. doi:10.1021/ja00462a012.

[95] J. K. Stolaroff, D. W. Keith, G. V. Lowry, Carbon Dioxide Capture from Atmospheric Air Using Sodium Hydroxide Spray, Environmental Science and Technology 42 (8) (2008) 2728–2735. doi:10.1021/es702607w.

[96] Y. J. Lin, E. Chen, G. T. Rochelle, Pilot plant test of the advanced flash stripper for CO_2 capture, Faraday Discussions 192 (2016) 37–58. doi:10.1039/c6fd00029k.

[97] P. M. Blauwhoff, G. F. Versteeg, W. P. Van Swaaij, A study on the reaction between CO_2 and alkanolamines in aqueous solutions, Chemical Engineering Science 38 (9) (1983) 1411–1429. doi:10.1016/0009-2509(84)80021-4.

[98] A. K. Saha, S. S. Bandyopadhyay, A. K. Biswas, Kinetics of absorption of CO_2 into aqueous solutions of 2-amino-2-methyl-1-propanol, Chemical Engineering Science 50 (22) (1995) 3587–3598. doi:10.1016/0009-2509(95)00187-A.

[99] C. Linkletter, D. Bingham, N. Hengartner, D. Higdon, K. Q. Ye, Variable selection for Gaussian process models in computer experiments, Technometrics 48 (4) (2006) 478–490. doi:10.1198/004017006000000228.

[100] A. Fisher, C. Rudin, F. Dominici, All models are wrong, but many are useful: Learning a variable's importance by studying an entire class of prediction models simultaneously, Journal of Machine Learning Research 20 (177) (2019) 1–81. arXiv:1801.01489.
URL http://jmlr.org/papers/v20/18-760.html

[101] R. L. Wasserstein, N. A. Lazar, The ASA's Statement on p-Values: Context, Process, and Purpose, American Statistician 70 (2) (2016) 129–133. doi:10.1080/00031305.2016.1154108.

[102] S. Greenland, S. J. Senn, K. J. Rothman, J. B. Carlin, C. Poole, S. N. Goodman, D. G. Altman, Statistical tests, P values, confidence intervals, and power: a guide to misinterpretations, European Journal of Epidemiology 31 (4) (2016) 337–350. doi:10.1007/s10654-016-0149-3.

[103] I. Hunt, Substituent Effects.
URL https://www.chem.ucalgary.ca/courses/350/Carey5th/Ch12/ch12-8b.html

[104] Y. Jing, E. M. Fell, M. Wu, S. Jin, Y. Ji, D. A. Pollack, Z. Tang, D. Ding, M. Bahari, M.-A. Goulet, T. Tsukamoto, R. G. Gordon, M. J. Aziz, Anthraquinone flow battery reactants with nonhydrolyzable water-solubilizing chains introduced via a generic cross-coupling method, ACS Energy Letters 7 (2021) 226–235.

[105] R. C. Kuczera, Z. P. Mourelatos, On estimating the reliability of multiple failure region problems using approximate metamodels, Journal of

Mechanical Design, Transactions of the ASME 131 (12) (2009) 1210031–12100311. doi:10.1115/1.4000326.

[106] C. Wang, K. Jiang, T. W. Jones, S. Yang, H. Yu, P. Feron, K. Li, Electrowinning-coupled co2 capture with energy-efficient absorbent regeneration: Towards practical application, Chemical Engineering Journal 427 (2022) 131981. doi:10.1016/j.cej.2021.131981.

[107] C. Wang, K. Jiang, H. Yu, S. Yang, K. Li, Copper electrowinning-coupled co2 capture in solvent based post-combustion capture, Applied Energy 316 (6 2022). doi:10.1016/j.apenergy.2022.119086.